FINAL REPORT
CONTRACT NAS 8-24788

HUGHES
HUGHES AIRCRAFT COMPANY

GRAVITY GRADIENT STUDY

JULY 1971

C.C. BELL

HUGHES RESEARCH LABORATORIES • MALIBU

HUGHES RESEARCH LABORATORIES
Malibu, California

a division of hughes aircraft company

GRAVITY GRADIENT STUDY

FINAL REPORT
Contract NAS 8-24788

C. C. Bell
Exploratory Studies Department

sponsored by
NATIONAL AERONAUTICS AND SPACE ADMINISTRATION
GEORGE C. MARSHALL SPACE FLIGHT CENTER
Huntsville, Alabama

SECTION I

INTRODUCTION

A. BACKGROUND

For the past several years, we have been engaged in a research and development program to demonstrate the feasibility of measuring mass distributions of the earth, moon, and other celestial bodies by detecting the spatial gradients of their fields from orbiting vehicles using rotating gravity gradiometers. In a continuing effort supported by internal HAC funding and a series of contracts with NASA and the Air Force, we have shown the engineering feasibility of the rotating gravity gradiometer concept through the design, fabrication, and demonstration of a laboratory research model which has the sensitivity required for many of the potential applications. We have also carried out a number of applications studies that show that this sensor will have significant scientific and engineering value in earth geodesy programs, both orbital and airborne, in the investigation of the asteroid belt, in the exploration of the outer planets and their satellites, and in future lunar exploration.

One of the important first steps in this continuing exploration program would be a detailed survey of the whole moon from spacecraft in very low orbits to obtain accurate, high resolution information on the terrain, elevation, electromagnetic field, and gravity field distributions. The attainment of a complete, high resolution gravity anomaly map early in the program will have a significant impact on all the future flights, for a detailed knowledge of both the frontside and the backside gravity field will enable the mission programmers to insert and maintain orbiting vehicles in very low orbits (less than 20 km) that could not be attempted with our present knowledge of the lunar gravity field. In addition, the high resolution maps of the gravity anomalies will suggest important future lander and rover target regions, and the precise

TABLE OF CONTENTS

LIST OF ILLUSTRATIONS

SECTION I

INTRODUCTION

A. BACKGROUND

For the past several years, we have been engaged in a research and development program to demonstrate the feasibility of measuring mass distributions of the earth, moon, and other celestial bodies by detecting the spatial gradients of their fields from orbiting vehicles using rotating gravity gradiometers. In a continuing effort supported by internal HAC funding and a series of contracts with NASA and the Air Force, we have shown the engineering feasibility of the rotating gravity gradiometer concept through the design, fabrication, and demonstration of a laboratory research model which has the sensitivity required for many of the potential applications. We have also carried out a number of applications studies that show that this sensor will have significant scientific and engineering value in earth geodesy programs, both orbital and airborne, in the investigation of the asteroid belt, in the exploration of the outer planets and their satellites, and in future lunar exploration.

One of the important first steps in this continuing exploration program would be a detailed survey of the whole moon from spacecraft in very low orbits to obtain accurate, high resolution information on the terrain, elevation, electromagnetic field, and gravity field distributions. The attainment of a complete, high resolution gravity anomaly map early in the program will have a significant impact on all the future flights, for a detailed knowledge of both the frontside and the backside gravity field will enable the mission programmers to insert and maintain orbiting vehicles in very low orbits (less than 20 km) that could not be attempted with our present knowledge of the lunar gravity field. In addition, the high resolution maps of the gravity anomalies will suggest important future lander and rover target regions, and the precise

knowledge of the gravity anomalies in the landing region will reduce the fuel margins required for a given targeting accuracy. An essential first element, therefore, in any future program of lunar exploration is the development of an orbiting gravity gradiometer to obtain the detailed gravity anomaly map.

We envision a spinning lunar orbiter inserted into a polar orbit at approximately 30 km altitude containing a high sensitivity, rotating gravity gradiometer with a fast time constant and its resonant frequency tuned to twice the spacecraft spin frequency and rotated by the spacecraft rotation. The data from both backside and frontside gravity gradient measurements would be stored in the spacecraft and transmitted to earth once every few days. In fourteen days the entire lunar surface would have been mapped to 30 km resolution. This data, since it is a direct measurement of the gravity field at the measurement point, needs merely to be coordinated with the satellite position data in order to obtain a gravity anomaly map and does not need the extensive data processing that doppler tracking data requires. With the new gravity map available, it is then possible to safely lower the vehicle orbit to 15 km or lower to obtain even higher resolution maps.

The following is a summary of what would be obtained from a completed lunar gravity gradiometer experiment. It can be seen that the applications that fall under the heading of engineering are at least as important as the science.

- EXPERIMENT OBSERVABLES

  Gravity gradient with threshold of less than 1 E. U. when spacecraft is in view from earth or out of view (includes backside).

  Absolute gravity is obtained by processing the above observations, and produces accuracy and resolution comparable to previous techniques, but includes the backside for the first time.

  Performance of the gradiometer instrument for engineering evaluations.

- SCIENCE OBJECTIVES AND EXPECTATIONS

Produce a gravity gradient and absolute gravity map of the entire lunar surface overflown by the spacecraft. This will be a band in latitude between + and - the value of spacecraft orbit inclination to the lunar equator. (Obviously, it is preferable to map from a polar orbit.)

The above gravity maps can then be correlated with visible features, particularly those backside basins and areas which differ so markedly from the frontside. We can expect the scientific implications for the backside to be substantial, perhaps even as significant as those for the frontside.

The above leads logically to physical interpretation of the results and their impact on the various theories of lunar history and formation. Judging from previous lunar gravimetric work and the effects it had on lunar science, we are safe in predicting dense, valuable scientific fallout from these observations.

The frontside observations provide an independent check of previous work.

It is likely that shape parameters for the mascons can be obtained, particularly since both gradient and absolute gravity are determined accurately.

Successful engineering evaluations of this new instrument, in a space and spacecraft environment not achievable on earth, may go a long way toward preparing this instrument for the earth-satellite or even aircraft applications with all of the ensuing implications for earth physics and earth resources.

- ENGINEERING OBJECTIVES AND EXPECTATIONS

The present errors in prediction of future spacecraft positions are due primarily to lack of lunar farside gravity data. This experiment will produce a dense coverage of the lunar backside.

With the data in hand, we can proceed to produce a gravitational model of the moon within the band overflown by the spacecraft which will significantly reduce the navigation errors noted above.

This should make possible the reduction of fuel expended in lunar landing maneuvers. It should permit pinpoint landing based upon earth-based tracking, allowing manned and/or unmanned precise landing. This could be of critical importance to future lunar exploration, and have cost and mission impacts of large magnitude.

The above capabilities in navigation affect mission safety, rescue, docking, landing accuracies, fuel consumption, and many other critical parameters.

B. OVERVIEW OF ACCOMPLISHMENTS TO DATE

1. Project History

The ultimate objective in the development of rotating gravitational gradient sensors is a class of small, lightweight, rugged sensors of high sensitivity and precision which may be used to measure accurately and rapidly the details of the gravity field during airborne or orbital surveys and as a component in an inertial guidance system to remove the effects of gravitational anomalies on the ultimate system performance.

The objectives of the initial research programs were to investigate the engineering feasibility of the basic concept, to develop sensor structures which would operate at a high sensitivity level both in free fall and in 1 g environment, to measure the sensor's sensitivity to gravitational fields, and to investigate the sources of noise produced by the rotation of the sensor. A torsionally flexible structure utilizing piezoelectric readout was found to be a suitable design and offers a significant improvement over other possible gradiometer designs. It has the capability of being operated in an earthbound laboratory environment while still maintaining the high sensitivity and signal-to-noise ratio required to measure gravitational gradients as low as 10^{-9} sec^{-2} (1 Eötvös unit (E. U.)). This combination of rugged construction and low threshold has been displayed in our experimental work. In 1965 gravitational gradient sensors were calibrated in the laboratory by means of a dynamic gravitational gradient generator and demonstrated a threshold sensitivity below 10^{-9} sec^{-2} (1 E. U.). Subsequently, in 1967, the sensor detected the gradients of stationary masses while rotating on a soft-mounted suspension. The present noise level of this sensor is ±1 E. U. (1 σ at an integration time of 10 sec).

During 1969 under Contract NAS 8-24788 for NASA, we carried out a study of the utilization of the rotating gravity gradiometer for mapping of the lunar gravity field. In addition to a spacecraft design study, we carried out an experimental simulation where we used lead masses to create gravity gradient fields that had exactly the same magnitude and time variation as the gravity gradient signals that would be expected from an orbiting vehicle around the moon. During the program we constructed and demonstrated a gravity gradiometer that resolved the gravity gradient signals of two closely spaced masses and measured a relative amplitude difference of 2 E. U. with time constants (3 to 10 sec) appropriate for lunar orbital measurements. This work is detailed in the contract report dated January 1970 and is summarized in the Appendix of this report (presented at the Symposium on Dynamic Gravimetry in March 1970).

2. Current Program

During the past year as a continuation to the above discussed NASA contract, we tested a laboratory model of a gradiometer with a 2 Hz resonant frequency. The purpose of this development was to determine sensor operability and stability. Preliminary tests were run on various types of piezoceramic materials to determine the material least affected by temperature.

A laboratory model of the sensor was assembled and run through various temperature cycle tests to establish the changes in resonant frequency, sensor Q, and scale factor with shifts in temperature. The tests showed a resonant frequency shift of less than 0.002 Hz/C^{o}. This frequency shift would cause a slight shift in scale factor, but using a low Q sensor (Q = 40 to 80) with thermistor monitoring of temperature data to ±0.1^{o}C, the scale factor shift could be easily calibrated out.

Q shifts for the sensor without resonant tuning were large (approximately 50% over the temperature range). However, with the appropriate tuned circuit on the sensor output, Q shifts were minimized and over a temperature range of 25^{o}C to 45^{o}C showed a maximum

deviation of ±5%. This scale factor error could also be easily calibrated out with temperature knowledge.

The sensor was then excited with rotating gravity gradient fields to test its long term stability at ambient temperature (uncontrolled room temperature approximately 72 ±2°F). The driving field was approximately 520 E. U. Results of these tests indicated that the amplitude (inphase) signal was quite stable over periods of up to 12 hours (rms drift over 12 hours was less than 10 E. U. and was assignable to a temperature shift of 1. 5°C over the duration of the test). There was, however, some phase shift due to slight changes in resonant frequency with temperature; this effect was very noticeable because of the high Q of the system and would be reduced if a lower Q sensor were used.

Low frequency acceleration noise was also evident and indicated the necessity of balancing future test models to improve their acceleration rejection capabilities.

SECTION II

TECHNICAL DISCUSSION

A. THEORY OF SENSOR OPERATION

The instrumentation used in this experimental program was the Hughes rotating gravitational gradient sensor. A laboratory model of this instrument is shown in Fig. 1, and a schematic of the method of operation is shown in Fig. 2.

The basic concept of the rotating gravitational gradient sensor is as follows. If a system of proof masses is rotated in the static gravitational field of an object, the gravitational force gradient of this field will induce dynamic forces on the proof masses with a frequency which is twice the rotation frequency of the system, while inertial effects caused by accelerations of the proof mass mounting structure will induce forces with a frequency at the rotational frequency. The strength and direction of the gravitational force gradient can be determined independently of the inertial forces by measuring the amplitude and phase of the vibrations induced in these proof masses at the doubled frequency. Analysis shows that the sensing of the gravitational gradient will still occur if the proof mass system is in free fall. More specifically, the proof mass system used is a system of masses coupled together with springs in a geometry which becomes a rotating differential angular accelerometer.

In general the gravitational field potential at a distance R from a mass point M is given by

$$\phi = - \frac{GM}{R} \quad , \tag{1}$$

where the universal gravitation constant $G = 6.67 \times 10^{-11}$ $m^3/kg\ sec^2$. The second order gradient of the gravitational potential is given by the symmetric tensor:

M 5704

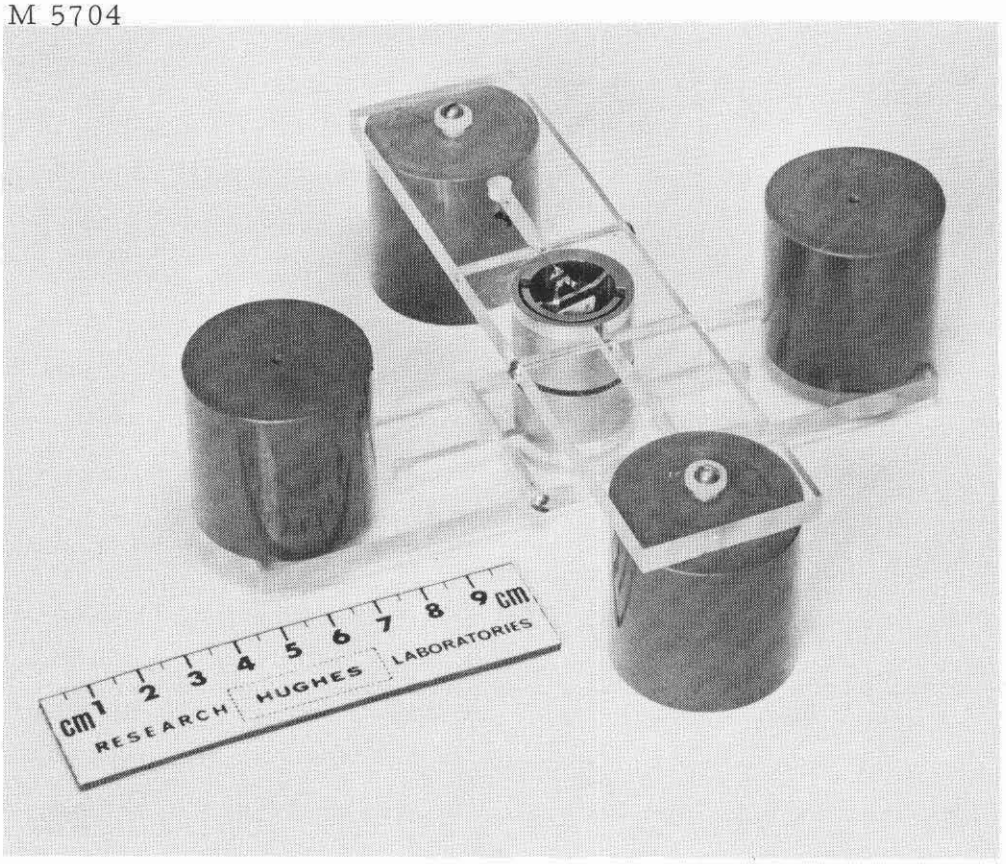

Fig. 1. Torsional Gravity Gradiometer.

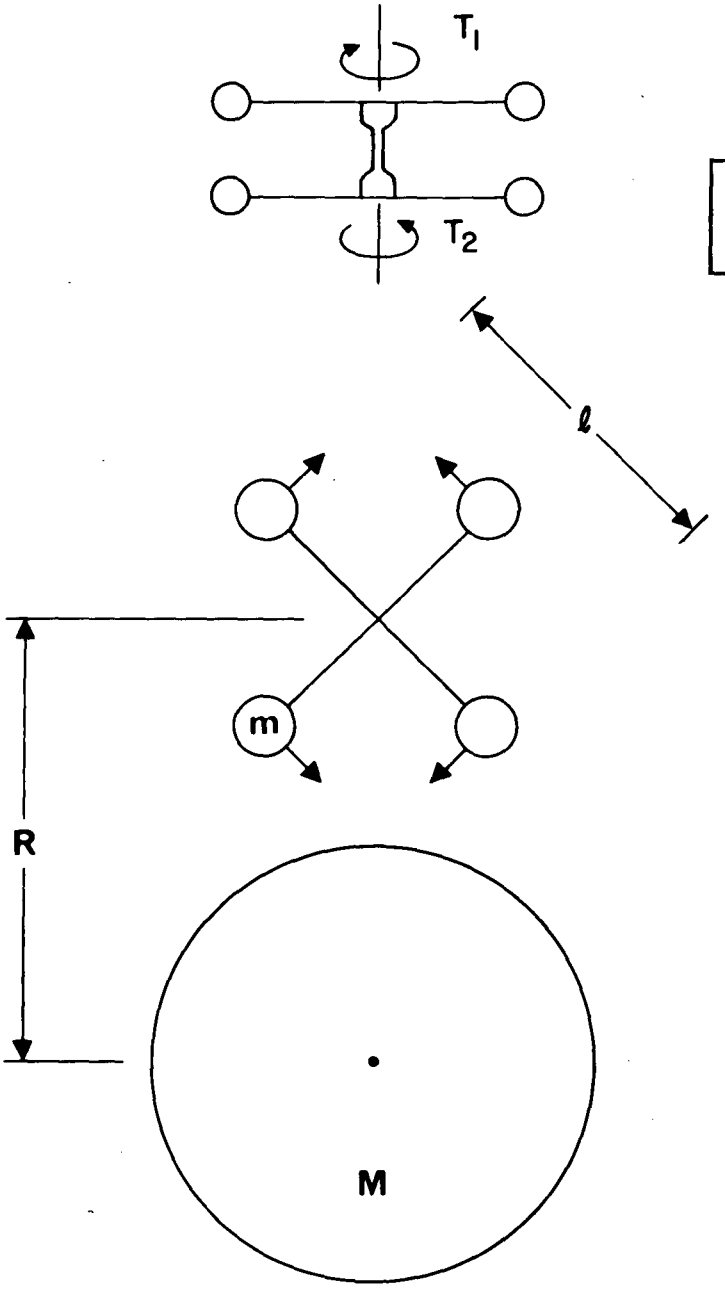

$$\frac{T_1 - T_2}{\theta} = \frac{3GMm\ell^2}{4R^3}$$

Fig. 2. Torsional Gradiometer in Free Fall.

$$\Gamma = \nabla(\nabla\phi) = \begin{pmatrix} \frac{\partial^2\phi}{\partial x^2} & \frac{\partial^2\phi}{\partial y \partial x} & \frac{\partial^2\phi}{\partial z \partial x} \\ \frac{\partial^2\phi}{\partial x \partial y} & \frac{\partial^2\phi}{\partial y^2} & \frac{\partial^2\phi}{\partial z \partial y} \\ \frac{\partial^2\phi}{\partial x \partial z} & \frac{\partial^2\phi}{\partial y \partial z} & \frac{\partial^2\phi}{\partial z^2} \end{pmatrix} \qquad (2)$$

or, in Fig. 2,

$$\Gamma = \nabla(\nabla\phi) = \begin{pmatrix} \Gamma_{xx} & \Gamma_{yx} & \Gamma_{zx} \\ \Gamma_{xy} & \Gamma_{yy} & \Gamma_{zy} \\ \Gamma_{xz} & \Gamma_{yz} & \Gamma_{zz} \end{pmatrix} = \frac{GM}{R^3} \begin{pmatrix} +2 & 0 & 0 \\ 0 & -1 & 0 \\ 0 & 0 & -1 \end{pmatrix}, \qquad (3)$$

when the x axis is aligned along the radius R.

The sensor rotates about its torsionally resonant axis through an angle $\theta = \omega t$, where ω is exactly one-half the torsional resonant frequency. A force analysis diagram of the sensor is shown in Fig. 3.

Only the torque between the sensor arms is coupled into the sensor output. This torque is given by

$$\Delta T = \frac{T_B - T_A}{2} = \frac{[(F_2 \times r_2) + (F_4 \times r_4)] - [(F_1 \times r_1) + (F_3 \times r_3)]}{2}, \qquad (4)$$

where

$T_A \equiv$ torque on arm A

$T_B \equiv$ torque on arm B.

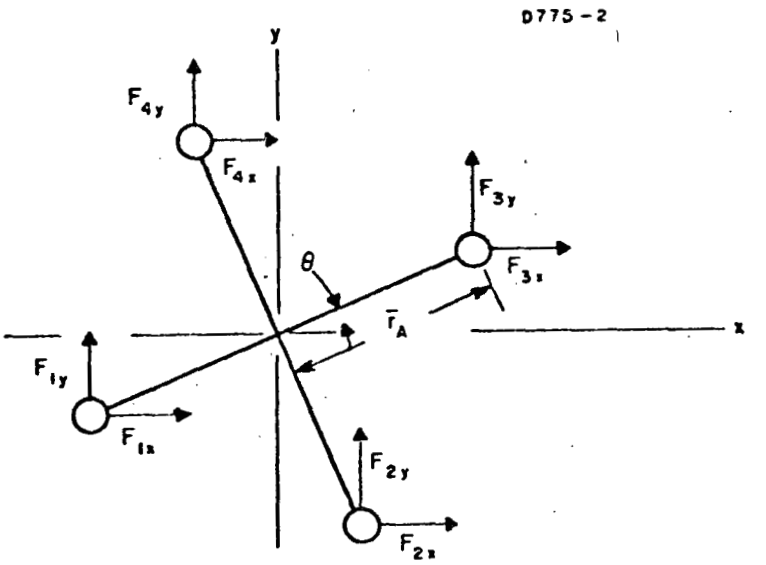

Fig. 3. Sensor Force Analysis Diagram.

If the forces on the ends of the arms are resolved into their x and y components and the indicated vector products are taken (arm A only),

$$T_A = mr\,[(a_{1x} - a_{3x}) \sin\theta + (a_{3y} - a_{1y}) \cos\theta] \quad , \tag{5}$$

where a_{1x}, a_{1y}, a_{3x}, and a_{3y} are the components of the gravitational acceleration field. If we assume that the field is linear over the dimensions of the sensor,

$$a_{1x} - a_{3x} = -\,2r(\Gamma_{xx} \cos\theta + \Gamma_{xy} \sin\theta) \quad , \tag{6}$$

where $\Gamma_{xx} \equiv (\partial a_x/\partial x)$ and $\Gamma_{xy} \equiv (\partial a_x/\partial y)$; similarly,

$$a_{3y} - a_{1y} = +\,2r(\Gamma_{yy} \sin\theta + \Gamma_{yx} \cos\theta) \quad , \tag{7}$$

where $\Gamma_{yx} = \Gamma_{xy}$ because of symmetry.

Substituting (6) and (7) in (5),

$$T_A = mr^2\,[2(\Gamma_{yy} - \Gamma_{xx}) \sin\theta \cos\theta + 2\Gamma_{xy}(\cos^2\theta - \sin^2\theta)] \; ; \tag{8}$$

substituting double angle identities,

$$T_A = mr^2[(\Gamma_{yy} - \Gamma_{xx}) \sin 2\theta + 2\Gamma_{xy} \cos 2\theta] \quad . \tag{9}$$

A similar analysis will show that

$$T_B = -\,mr^2[(\Gamma_{yy} - \Gamma_{xx}) \sin 2\theta + 2\Gamma_{xy} \cos 2\theta] \; ; \tag{10}$$

finally

$$\Delta T = \frac{T_B - T_A}{2} = mr^2\,[(\Gamma_{yy} - \Gamma_{xx}) \sin 2\omega t + 2\Gamma_{xy} \cos 2\omega t] \quad , \tag{11}$$

where $\theta = \omega t$.

Using the values for Γ_{xx} and Γ_{yy} of (3) in (11), we may now evaluate the differential torque as

$$\Delta T = - \frac{6GM\, mr^2}{2R^3} \sin 2\omega t \quad , \tag{12}$$

or substituting the characteristic length of the sensor $\ell = 2r$,

$$\Delta T = \frac{3}{4} \frac{GM\, m\ell^2}{R^3} \sin 2\omega t \quad . \tag{13}$$

The angular resonant deflection between the two quadrupoles of the sensor rotating at one-half its torsional resonant frequency $\omega_n = 2\omega$ with an associated quality factor Q is therefore

$$\delta = \frac{2\Delta TQ}{I\,\omega_n^2} = \frac{3GMQ}{R^3\,\omega_n^2} \sin \omega_n t \quad , \tag{14}$$

where $I = m\ell^2/2$ is the quadrupole inertia.

The angle δ is extremely small. Surface gradients produced by the moon (1800 E. U.) will produce angular deflections of $\approx 5 \times 10^{-7}$ rad in the 2 Hz torsional sensor design (Q = 300, ω = 6 rad/sec), while useful threshold signals of 1 E. U. produce angular responses of $\approx 10^{-10}$ rad.

It is now necessary to transduce this mechanical motion into an electrical signal for processing and transmission. This is accomplished by using a flexural pivot as the torsional spring and affixing a barium titanate strain transducer to one of the flexural spring leaves (see Fig. 4). These transducers have been found to be more than adequate for sensing these small strains.

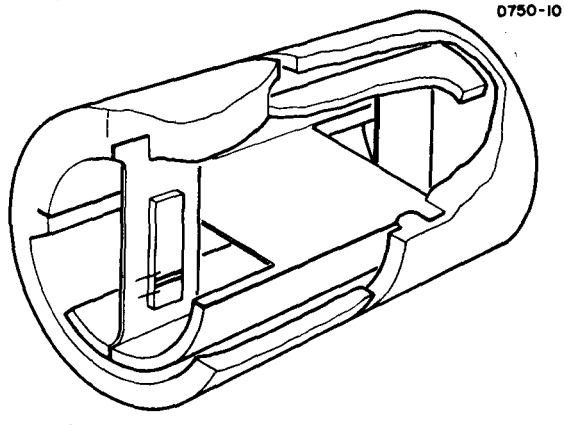

Fig. 4.
Typical Flexural
Pivot.

B. ELECTRONIC COUPLING INTO SENSOR

1. Theory

In order to optimize the coupling between the sensor and the first stages of amplification to obtain an improved signal-to-noise ratio, we have used a passive matching circuit to cancel out the capacitive reactive impedance of the piezoelectric strain transducers. This allows the input of the preamplifier to couple directly to the mechanical impedances of the sensor structure itself and lowers the effective impedance levels of the entire system, giving it less susceptibility to pick up and lower Johnson noise.

The equivalent electromechanical circuit for the sensor and the piezoelectric circuit without matching can be represented by the illustrated circuit (see Fig. 5) where I, S, and D are the inertia, spring constant, and damping of the sensor structure itself, $T_\Gamma = I\Gamma$ is the driving torque, and T_T is the random thermal torque driving the structure, C_g is the inherent capacitance of the transducer, R_A is the preamplifier load impedance, and K is the effective coupling of the piezoelectric transducer. The transducers can be represented by a transformer with a turns ratio of K:1 where the K transforms from electrical quantities to mechanical quantities at the same time it is changing impedance levels. We can eliminate the transformer coupling from the equivalent circuit by converting the mechanical components to their equivalent electrical components (see Fig. 6(a)).

The addition of the tuning tank circuit paralleling the transducer output is reflected in the circuit diagram of Fig. 6(b).

The equivalent electrical parameters of each circuit may be determined by measuring the frequency and Q of the sensor resonance both with and without the tuning circuit and, in addition, measuring the frequency and Q of the tuning circuit alone. This latter test is performed by the circuit shown in Fig. 7.

Starting with the data from the electronic tuning circuit alone

$$R_L = \omega L_E Q_E \tag{15}$$

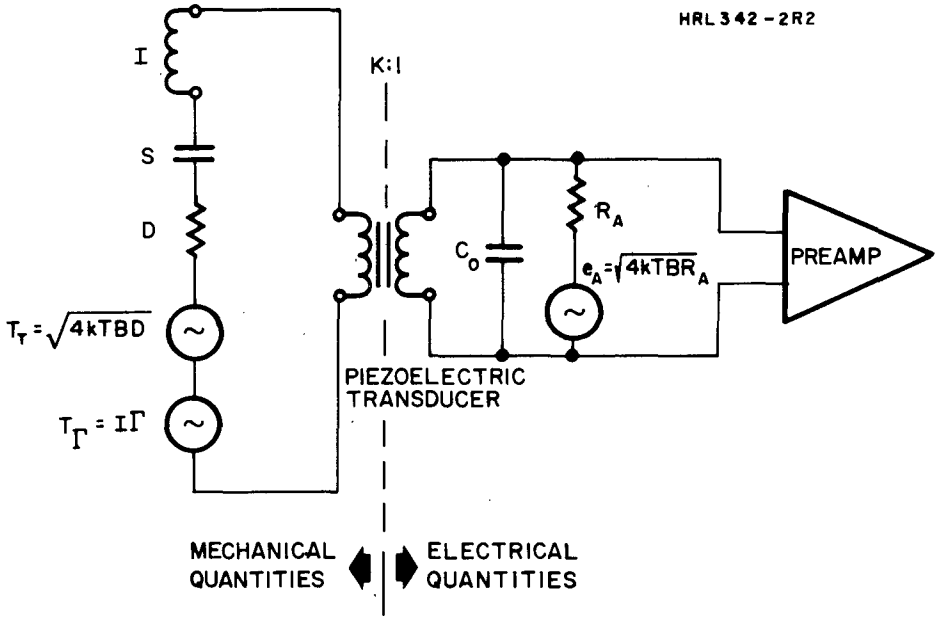

Fig. 5. Schematic of Sensor, Transducer, and Preamplifier.

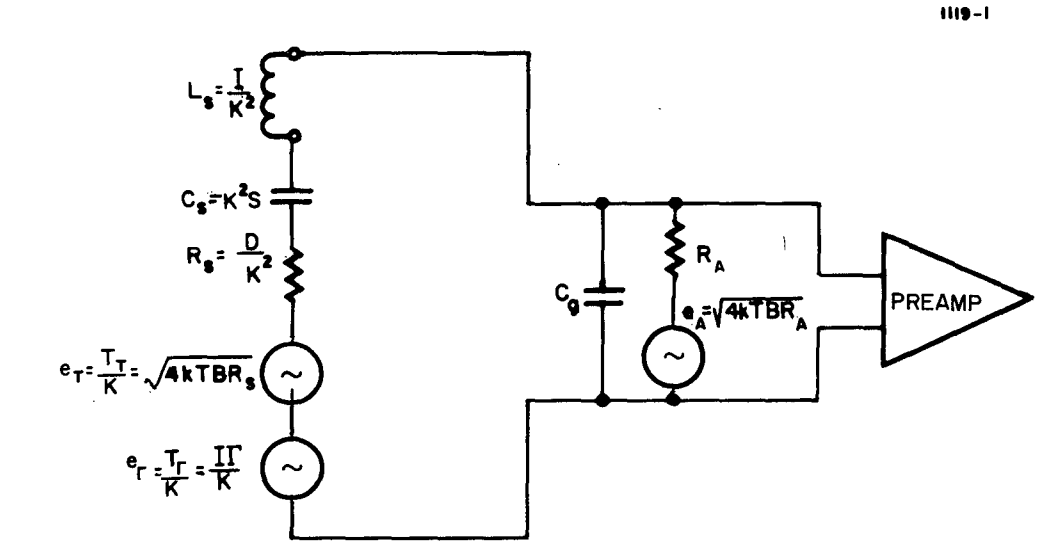

(a) untuned

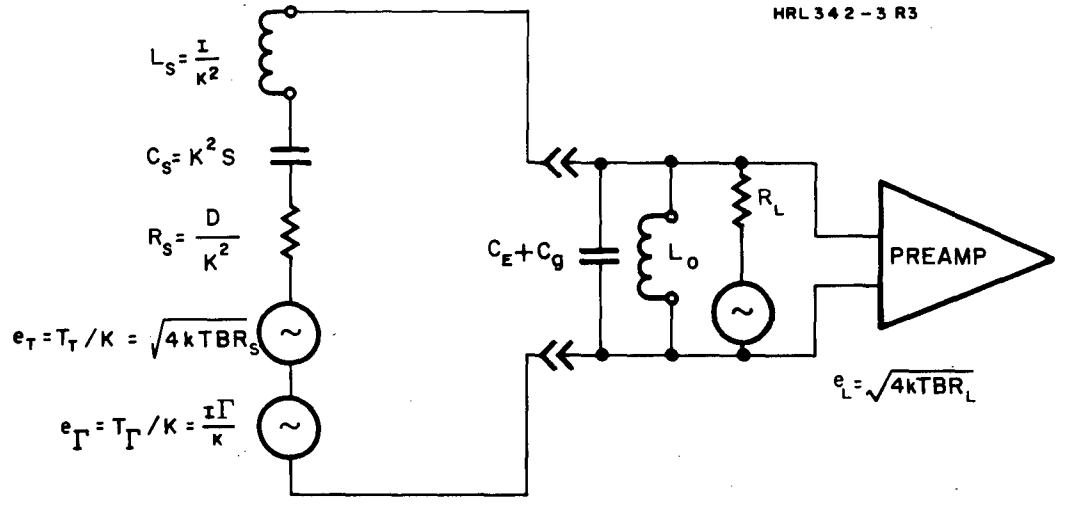

(b) tuned

Fig. 6. Equivalent Electrical Circuit of Sensor and Electrical Input Circuit.

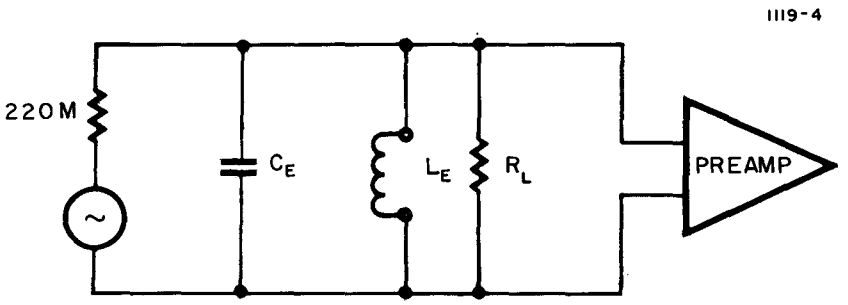

Fig. 7. Electrical Q Test Circuit.

where R_L is the equivalent parallel load resistance of the coil and amplifier. This resistance is not changed by the addition of the sensor equivalent circuit to the tuning circuit as shown in Fig. 6(b). The circuit of Fig. 6(b) has a Q given by

$$Q_T = \frac{\omega L_s}{R_s + R_L} \quad , \tag{16}$$

and the untuned circuit Q (Fig. 6(a)) is

$$Q_u = \frac{\omega L_s}{R_s} \quad , \tag{17}$$

where the contribution of the amplifier resistor (R_L) to the untuned resonant resistance is assumed to be small.

These two equations may be combined and solved for R_s

$$R_s = \frac{R_L}{\frac{Q_u}{Q_T} - 1} \quad , \tag{18}$$

and we may then solve for L_s

$$L_s = \frac{Q_u R_s}{\omega} \quad ,$$

and sensor capacitance

$$C_s = \frac{1}{\omega^2 L_s} \quad . \tag{19}$$

Sensor gauge capacitance C_g, and the tuning capacitance C_E can be measured directly.

Once all the components are known, the resonant impedances may be determined, the thruput of each circuit may be calculated, and the noise voltage outputs due to resistive components may be determined.

Figure 8 shows the equivalent untuned circuit at resonance.

Since all the impedances of this circuit are now known, the contribution of each noise source to the voltage output may be determined and statistically summed to obtain a total noise output figure. Similar

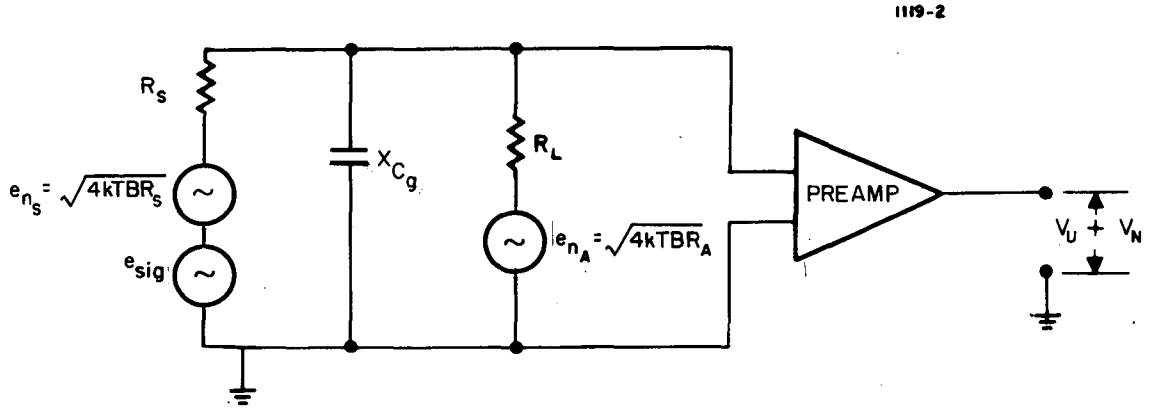

Fig. 8. Untuned Circuit at Resonance.

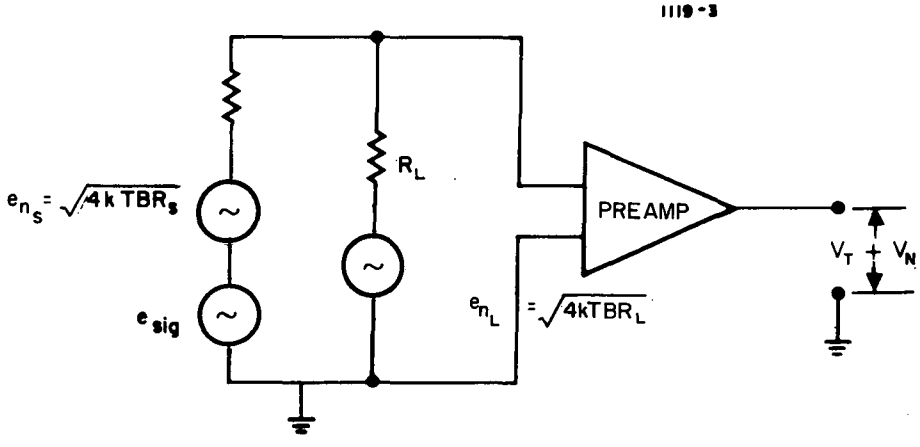

Fig. 9. Tuned Circuit at Resonance.

calculations may be used to determine the noise figure of the tuned resonant circuit which simplifies to Fig. 9 at resonance. The signal-to-noise ratio for each circuit may then be determined and compared.

2. Experimental Results

Tests were performed on the 2 Hz sensor as outlined in the above section using an electrical drive input. The experimental data are given below:

$Q_u = 167$ $\quad L_E = 36,500$ Hz

$Q_T = 115$ $\quad C_E = 0.169$ mF

$Q_E = 15$ $\quad C_g = 8 \times 10^{-9}$ F; $X_{C_g} = 10$ MΩ

$V_u = 420$ mV $\quad f_n = 2.03$ Hz

$V_T = 280$ mV $\quad R_A = 20$ MΩ

Using the equations developed in the previous section, the sensor electrical equivalents may be calculated with results as follows:

$$R_L = 7 \text{ M}\Omega$$

$$R_s = 16.3 \text{ M}\Omega$$

$$L_s = 2.14 \times 10^{8} \text{ H}$$

$$C_s = 2.76 \times 10^{-12} \text{ F} \ .$$

To prove the validity of the model we can now calculate the expected ratio of output voltages and compare this calculation to the measured ratio

$$\left(\frac{V_U}{V_T}\right)_{\text{measured}} = 1.50$$

$$\left(\frac{V_U}{V_T}\right)_{\text{calculated}} = 1.40 \ .$$

Since these ratios are within 10% of each other the validity of the model is assumed.

As mentioned in Section III-C-1, the sensor had only one active readout gauge, the other having been broken during assembly. The signal-to-noise ratios calculated for this sensor are contained in the first column of Table 1. We can also compare this signal-to-noise ratio to the ratio we would obtain if both gauges were operating. With both gauges the sensor resistor would be reduced by a factor of 4, to 4 MΩ and the gauge capacitance would have doubled or the gauge impedance would have been lowered to 5 MΩ. These new impedance values imply an untuned Q of 40 and a tuned Q of 14.5.

TABLE I

SIGNAL-TO-NOISE 2 Hz SENSOR

	1 Gauge	2 Gauges
Total Noise Tuned	47.5 nV	64.0 nV
Noise Untuned	32.0 nV	45.1 nV
Signal Tuned	280 mV	500 mV
Signal Untuned	420 mV	645 mV
Unfiltered		
$(S/N)_T$	5.9×10^6	7.8×10^6
$(S/N)_u$	13.1×10^6	14.3×10^6
Filtered (26 seconds)		
$(S/N)_T$	8.9×10^6	86×10^6
$(S/N)_u$	13.1×10^6	57.3×10^6

Table I shows the comparative results. Note that the tuned S/N shows little improvement until it is filtered to the same integration time, in this example 26 sec (Q = 166). It should also be noted that doubling of the number of gauges increases the signal to noise by a factor 4 in the untuned sensor and by a factor of 10! in the tuned sensor.

The noise figure on the tuned sensor with two gauges is approximately the thermal noise limit (0.3 E.U. at 2 sec (Q = 14.5) or 0.03 E.U. at 20 sec).

SECTION III

DISCUSSION OF EXPERIMENTS

A. EXPERIMENTAL GOALS

The goal of this contract research was to design a 2 Hz resonant frequency breadboard gravity gradiometer and to determine its noise threshold and scale factor when operated in both a vertical and horizontal position. An additional purpose was to determine the effect of temperature on scale factor, consequent signal phase, and amplitude drift.

Data on the temperature tests are contained in Section III-C-1; the noise, drift, and scale factor data are reflected in Section III-C-2.

B. COMPONENTS DESIGN

1. Transducer Material

Tests were run on two different types of piezoceramic materials to determine if either material showed preferred characteristics with variations in temperature. The materials tested were barium titanate (material of Gulton SC-4 strain transducers used on the 31 Hz sensor) and lead zirconium titanate (Glennite G-1500 and Clevite PZT-5B). Although the manufacturer's data on barium titanate indicated considerable variation in piezoelectric charge coefficients, versus temperature in the room temperature region and the lead zirconium titanate compounds did not, there was little experimental difference between the materials in output variation of the transducers versus temperature.

All three materials exhibited a similar, slight degradation of the output signal with temperatures in the range of 20°C to 45°C with the exception of one of the G-1500 strain transducers (see Fig. 10). This test indicated that variation of transducer material properties with temperature does not significantly affect the output of the sensor. The variation between transducers of the same material was greater than the variation between materials.

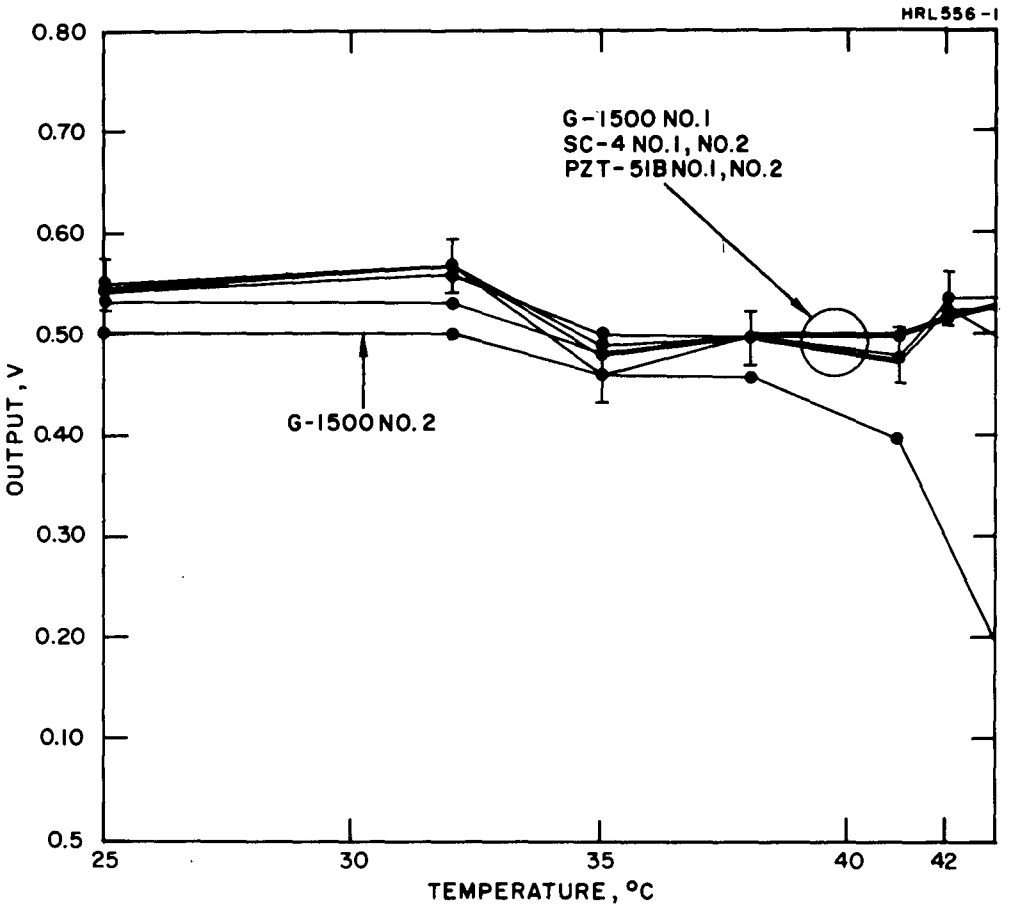

Fig. 10. Transducer Temperature-Output Data.

Results of these tests indicate that consideration should be given to a consistent method of bonding the transducer to the flexure leaf. However, funding did not permit such an investigation, and it was decided to build the sensor using the current bonding technique of cementing the transducers with Gulton transducer cement.

2. Flexure Design

Because of the requirements of low torsional spring rate and large transducer area, the available Bendix flexures were not satisfactory. It was decided to design a torsional flexure geometrically similar to the Bendix design but of a much larger diameter to accommodate the mounting of large area transducers. Sensor arm inertia (0.1357 lb-in.-sec^2) and end spring stiffness (0.817 in. lb/rad) were chosen. Using the design curves of Fig. 11 it was established that the central flexure should have a total stiffness of between 9 to 10 in. lb/rad.

Standard beam bending formulae were then used to determine flexure leaf size. Design calculations were performed for both aluminum and stainless steel, and parts were ordered to assemble both an all-aluminum and an all-steel flexure. It was decided to use the aluminum flexure in the final assembly in order to minimize changing stresses that would occur between the aluminum pivot and the aluminum arms with varying temperatures.

3. Sensor Design

The sensor design was based on the torsionally resonant designs which have been used in previous Air Force and NASA work. However, because of the low resonant frequency required, considerable structural modification on the sensor was necessary.

The sensor arms were elongated, heavier end masses were added, and Bendix flexures were used as end pivots. As already mentioned, the central flexure was modeled after the Bendix design but was two inches in diameter, in order to accommodate larger transducers.

The sensor case and frame designs were modified accordingly to fit this new sensor.

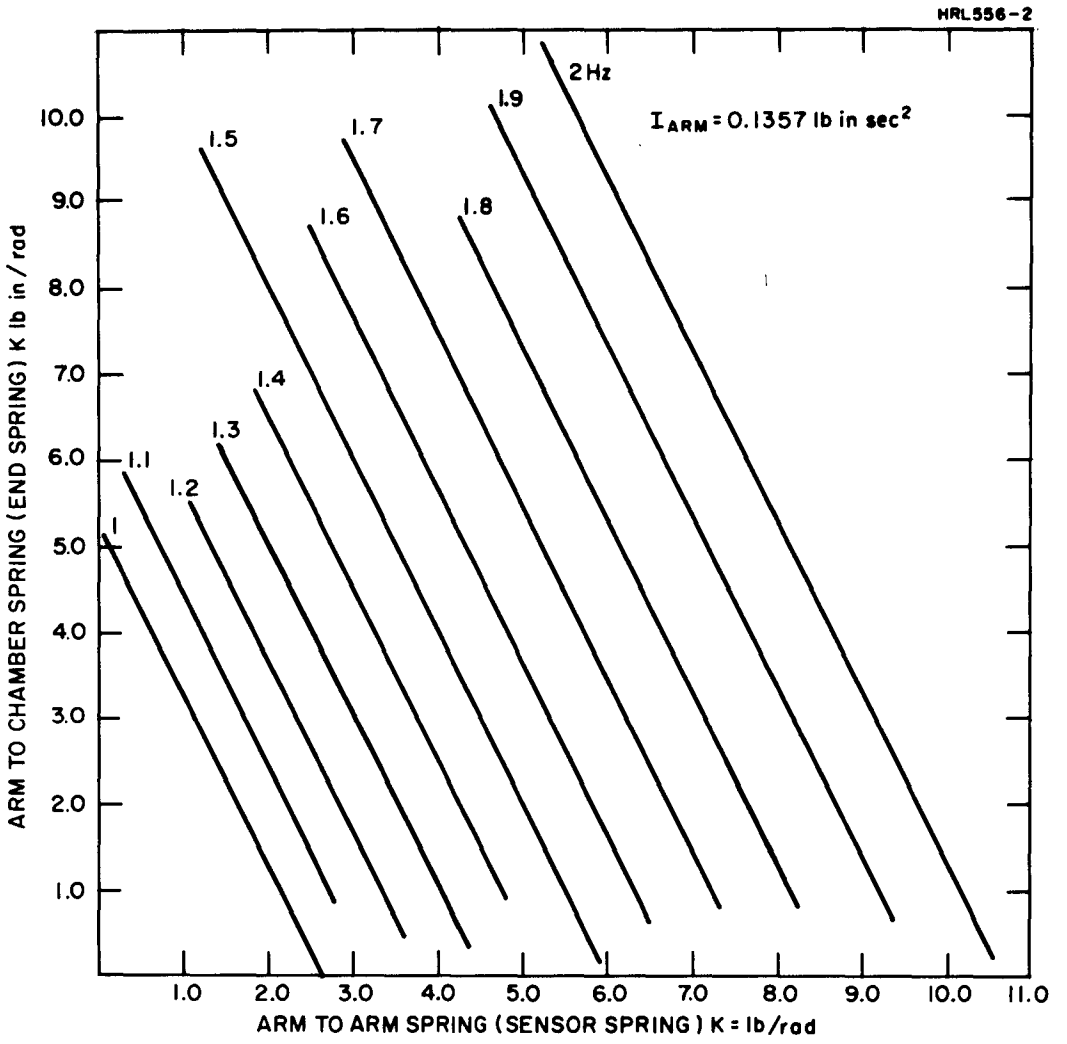

Fig. 11. Flexure Spring Rate Design Curves.

An exploded view of this sensor is shown in Fig. 12 and the assembled sensor is shown in Fig. 13 (without the surrounding vacuum chamber).

The sensor arm length is 4.250 in. and the end masses weigh 438 grams each. The calculated arm inertia is 0.1357 lb-in.-sec^2 (including the self-inertia of the arms and masses). The end pivots are Bendix flexures P/N 5008-600 with a torsional spring rate of 0.817 in. lb/rad. The spring rate of the central flexure is designed to be 9.4 in. lb/rad (including transducers).

The expected natural frequency of the design was 2.0 Hz(±5%).

Actual resonant frequency measured in the laboratory was nominally 2.04 Hz.

4. Amplifier Design

A schematic of the amplifier design is shown in Fig. 14.

This amplifier was tested to determine its noise level using the same test setup and signal detection electronics as used to obtain the sensor noise and drift data — discussed in Section III-C-2.

A noise trace is shown in Fig. 15. The rms value of the electronics noise level is less than 0.1 E.U., integrating over a 10 sec time constant.

After being amplified the signal was processed through a Princeton Applied Research Lock-In Amplifier (Model 121), where it was phase detected using a signal from the rotating gravity generator at twice the rotation speed as a reference. Because of the high level of acceleration noise in the sensor, the Lock-In amplifier was operated with a 100 sec integration time. Data from the Lock-In amplifier was recorded on an X-Y recorder.

C. SENSOR EXPERIMENTS

1. Temperature Tests

After assembly of the sensor and support frame, a series of temperature tests were run on the sensor to determine the effect of temperature on sensor resonant frequency Q and output voltage.

M 7446

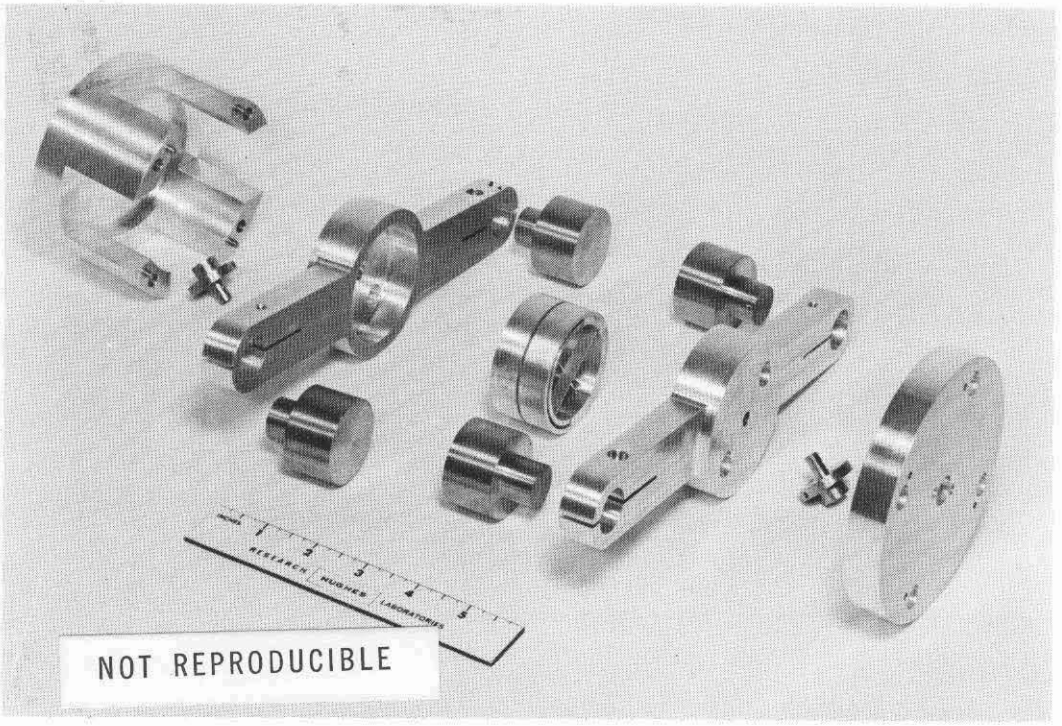

Fig. 12. Exploded View of 2 Hz Sensor.

M7447

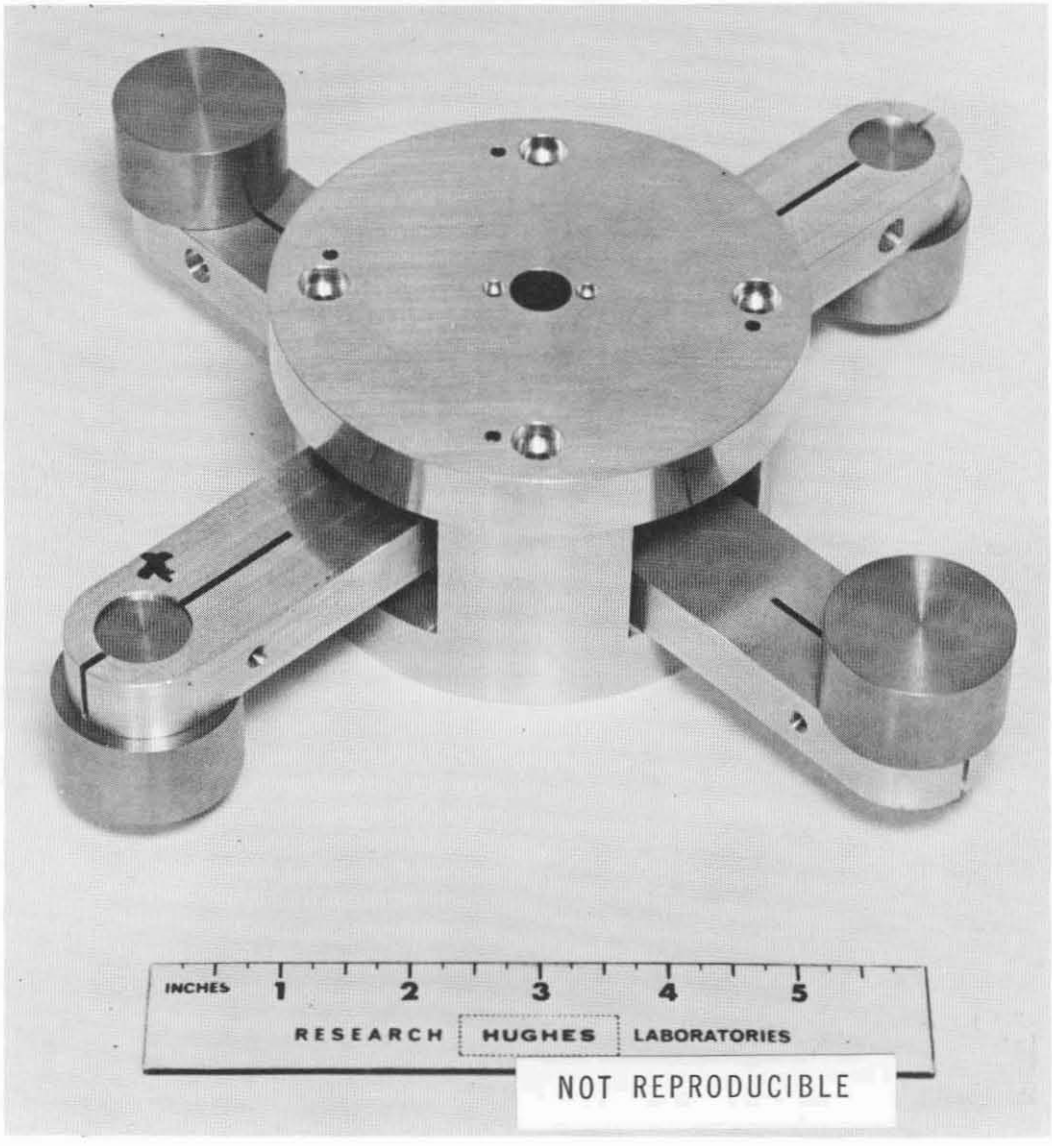

Fig. 13. 2 Hz Sensor Assembly.

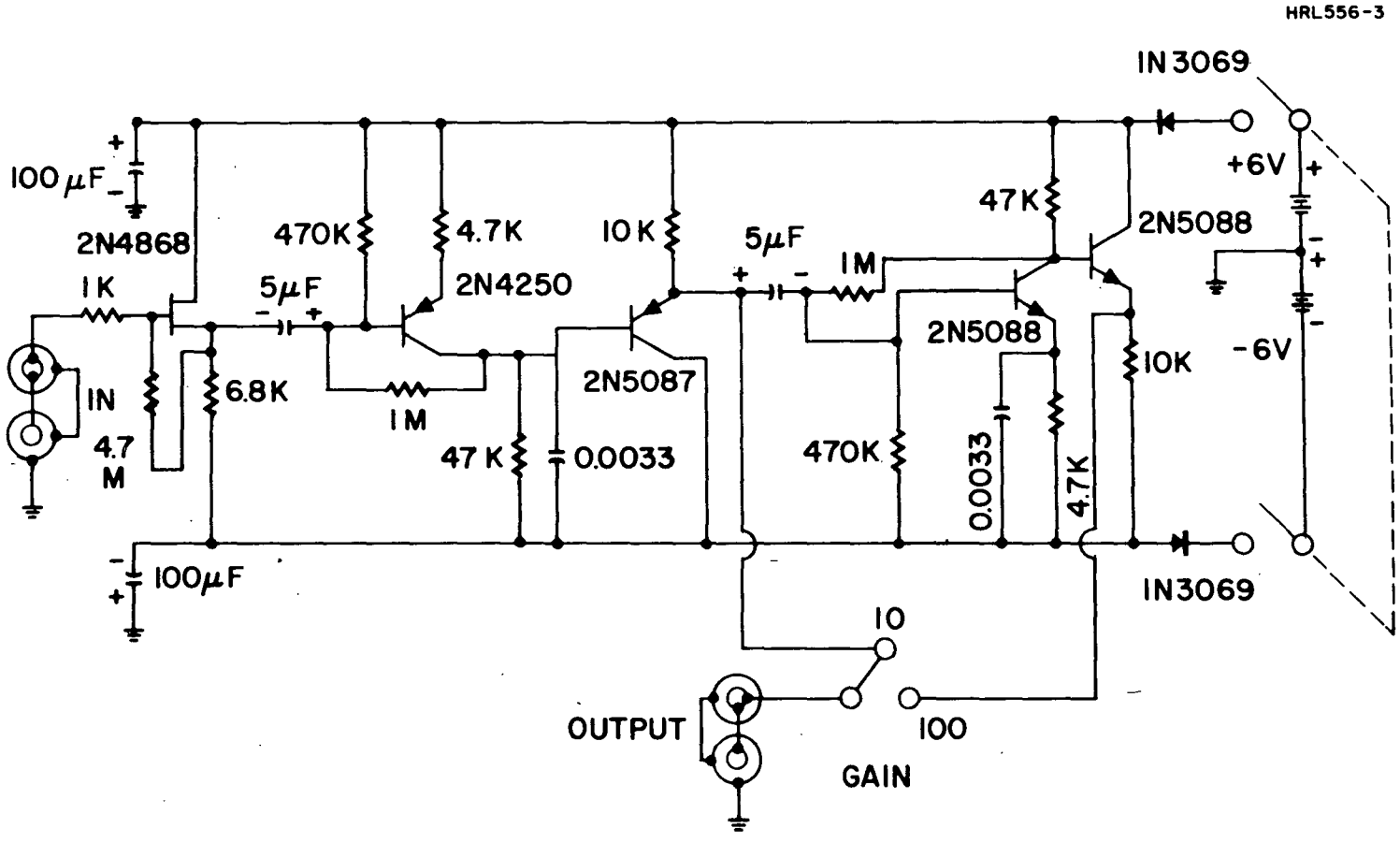

Fig. 14. Low Frequency Amplifier.

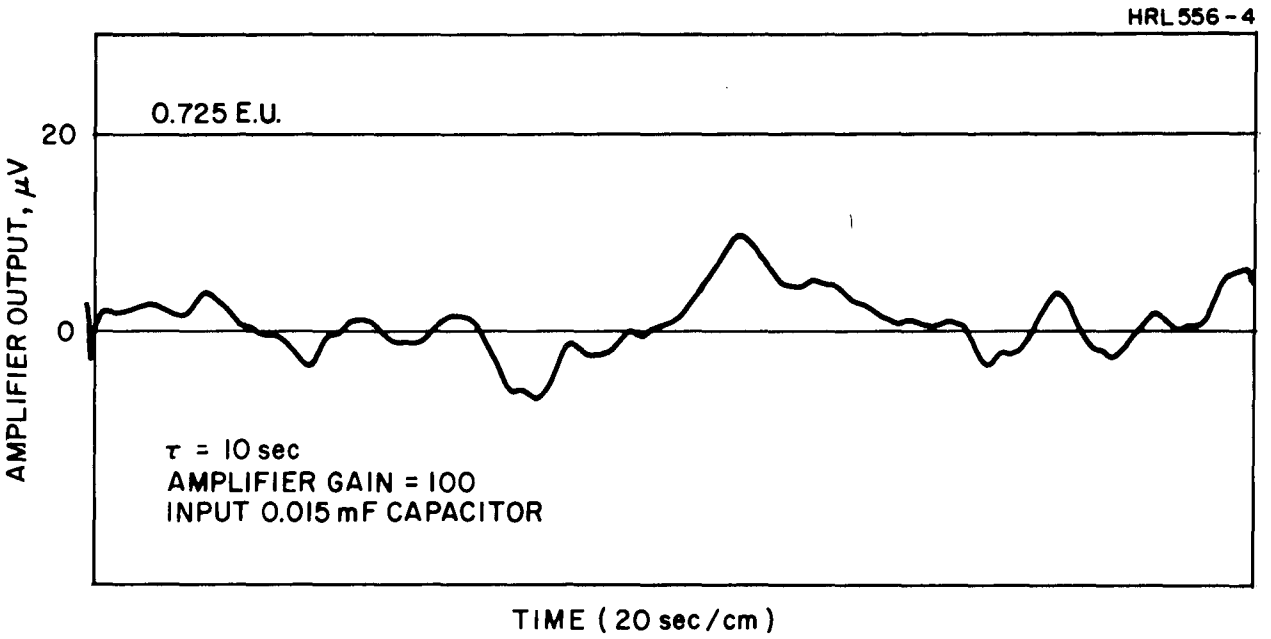

Fig. 15. Amplifier Noise Level.

The sensor was placed in an expanded styrofoam ice chest that was fitted with proportionally controlled resistance heating elements mounted on large heat sinks. Temperature control of the chamber was maintained to better than 0.1°C by this system. The sensor was fitted with three piezoelectric transducers (PZT-5B). Two of these transducers (the output transducers) were mounted on the end leaves of the central flexure, these transducers were full size covering the entire area of the leaf (1.5 in. x 0.25 in. x 0.010 in.). A half-length transducer (0.75 in. long) was mounted on the center leaf of the flexure to be used as a driving transducer. Unfortunately, during assembly, one of the output transducers was broken. It was decided to continue using only one output transducer. The resulting higher output impedance of the sensor degraded the noise level of the sensor slightly but did not significantly affect the test results.

During the temperature test, data was taken by driving the short transducer with the output of a General Radio coherent decade frequency synthesizer. The synthesizer is capable of being swept through a frequency range by the external application of a dc voltage ramp. The slope of the ramp determines the rate of frequency shift. Care was taken to assure that the frequency sweep rate was slow enough to allow for the fully integrated response of the sensor.

The frequency was swept over a 0.04 Hz band centered about the sensor resonant frequency. Q curves were run at four temperatures between 24°C and 60°C with the spin axis of the sensor oriented to both the vertical and horizontal.

Another set of data was run with a high impedance inductor (37,000 H) in parallel with the output of the transducers. (For a discussion of the theory of operation of this tuned circuit, refer to Section II-B.) Test data revealed no significant difference between the tests performed with the horizontal and vertical torsional axes.

It is interesting to compare the operation of the system with and without the tuned circuit on the sensor output. Figures 16, 17 and 18 show these comparisons for sensor Q, natural frequency, and voltage output. The most significant thing to note in these data is the reduction

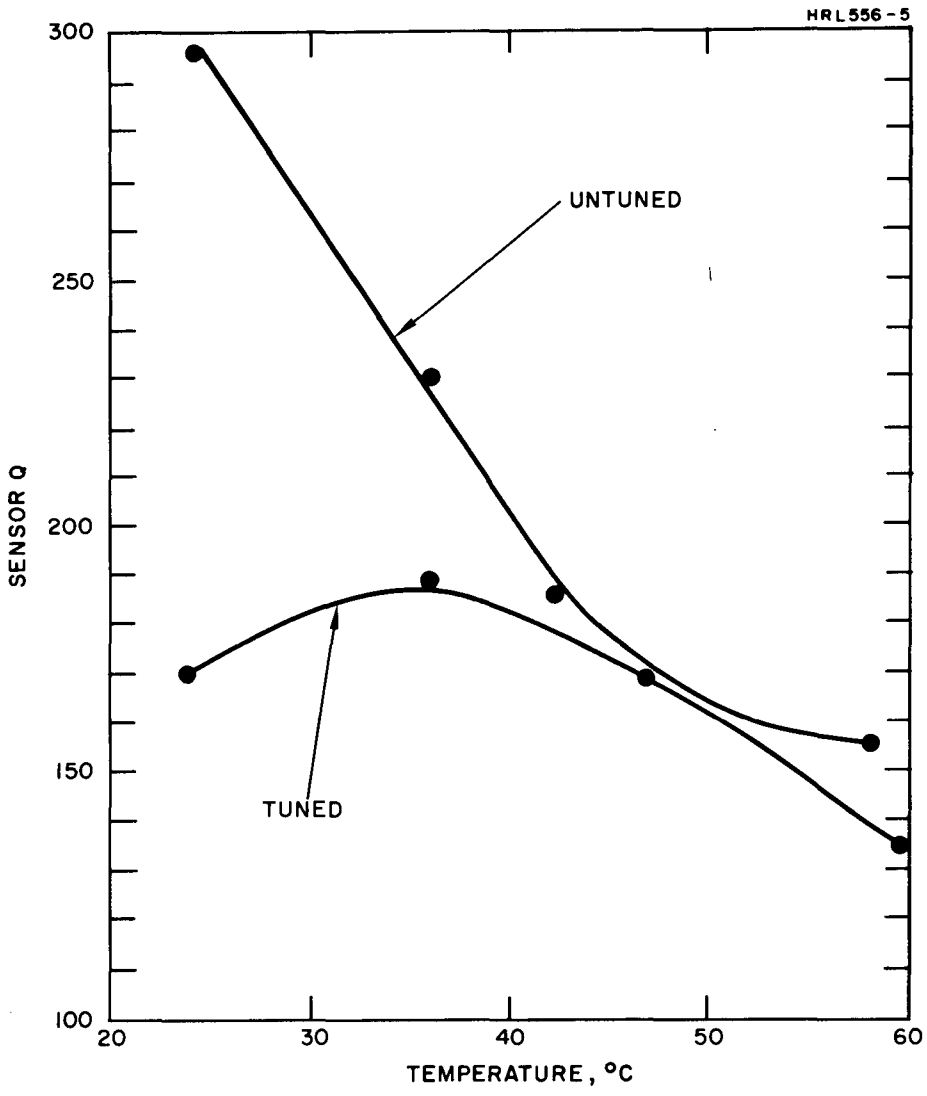

Fig. 16. Sensor Q as a Function of Temperature.

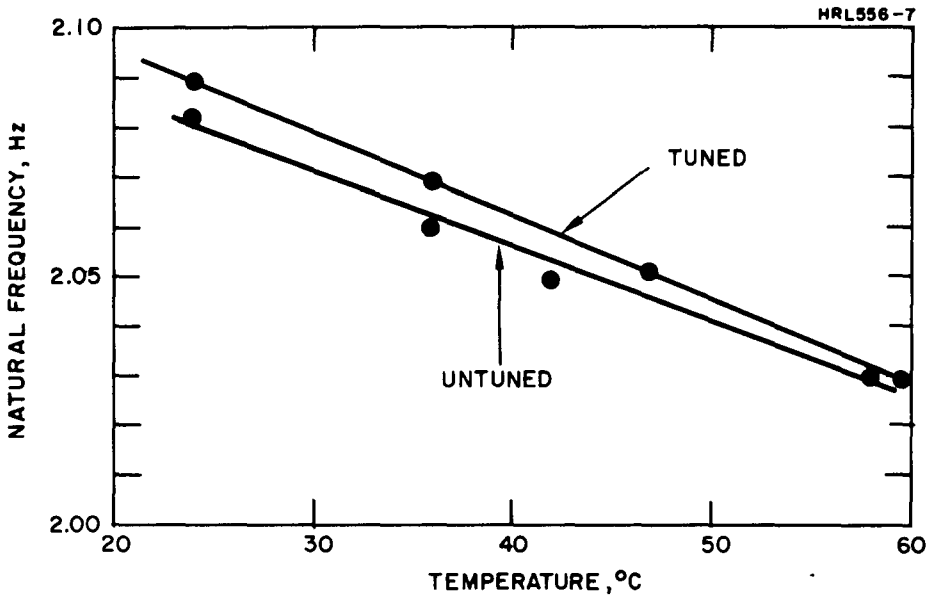

Fig. 17. Sensor Natural Frequency as a Function of Temperature.

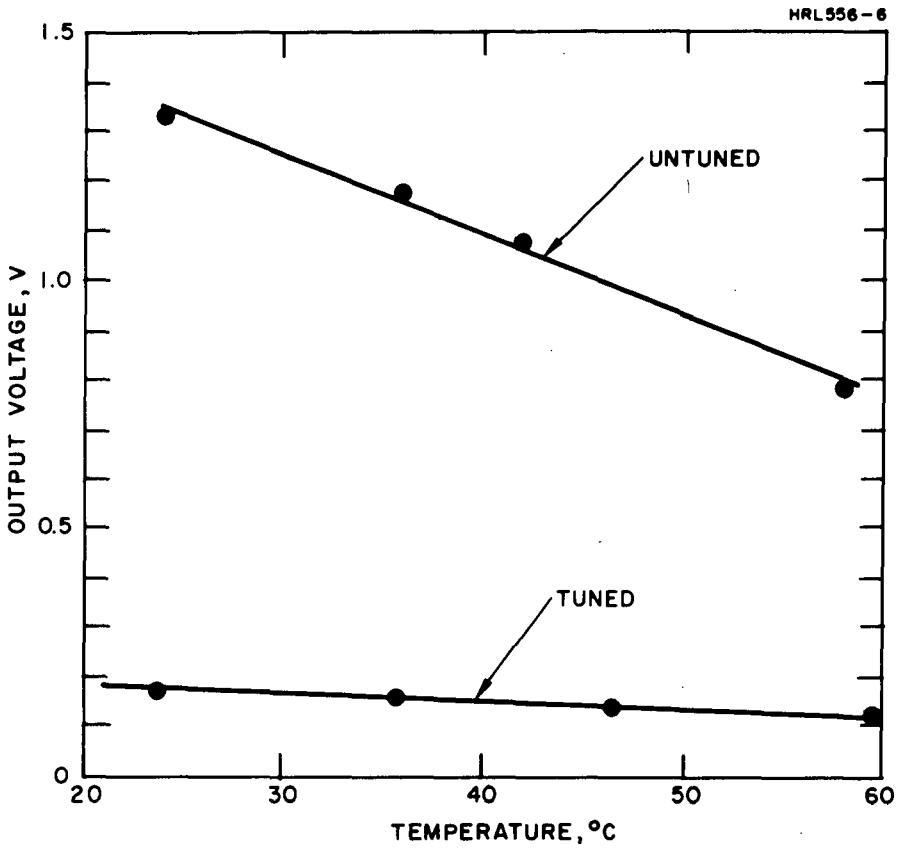

Fig. 18. Sensor Voltage Output as a Function of Temperature.

of variation of Q with temperature by use of the tuned circuit. Overall percent change in Q was reduced from nearly 60% to 10% (of the mean Q in the temperature range).

Note, however, that the addition of the tuned circuit did not significantly affect the variation of natural frequency with temperature.

The output voltage of the sensor was reduced by a factor of five with the addition of the tuned circuit. The percent variation of this output signal remained unchanged, however.

Note that the effect of temperature on these three parameters is linear in the range of interest, with the exception of the variation of Q in the tuned sensor.

The significant characteristics of these data are summarized in the following table.

TABLE II

SENSOR PARAMETER VARIATION WITH TEMPERATURE

Parameter	Range (24°C-50°C)		Slope	
	Untuned	Tuned	Untuned	Tuned
Sensor Q	295 - 165	190 - 160	-6.05/°C	0 at 35°C +2.8 at 24°C
Natural Frequency	2.09Hz-2.03Hz	2.08Hz-2.03Hz	-0.0015Hz/°C	-0.0015Hz/°C
Voltage Output	1.33V -0.93V	0.255V-0.178V	-0.0154V/°C	-0.00296V/°C

We can now use the natural frequency, amplitude drift, and Q drift with temperature to calculate the nominal amplitude and phase shift with temperature, assuming the operating speed is initially chosen at one-half the sensor resonant frequency ($\phi = 90^{\circ}$).

- PHASE ANGLE SHIFT

The phase angle is given by

$$\tan \phi = \frac{\frac{c\omega}{k}}{1-\left(\frac{\omega}{\omega_n}\right)^2} \quad , \tag{20}$$

and the sensor $Q = I\omega/c$; $c = I\omega/Q$; therefore, at resonance

$$\frac{c\omega}{k} = \frac{I\omega^2}{kQ} \quad \text{but} \quad \frac{I}{K} = \frac{1}{\omega_n^2} \quad .$$

Therefore,

$$\frac{c\omega}{k} = \frac{1}{Q}$$

or substituting in (20)

$$\tan \phi = \frac{1}{Q}\left[\frac{1}{1-(\frac{\omega}{\omega_n})^2}\right] = \frac{\omega_n^2}{Q(\omega_n^2 - \omega^2)} \quad . \qquad (21)$$

We will now differentiate both sides of this equation with temperature and temporarily let the right side of the equation be equal to a/b,

$$(a = \omega_n^2, \quad b = Q(\omega_n^2 - \omega^2))$$

$$\frac{d}{dT}(\tan \phi) = \frac{d}{dT}\left(\frac{a}{b}\right)$$

$$\sec^2 \phi \ \frac{d\phi}{dT} = \frac{b(\frac{da}{dT}) - a(\frac{db}{dT})}{b^2} \quad ,$$

but

$$\sec^2 \phi = \frac{b^2 + a^2}{b^2} \quad .$$

Therefore,

$$\frac{d\phi}{dT} = \frac{b\frac{da}{dT} - a\frac{db}{dT}}{b^2 + a^2} \quad .$$

Now

$$\frac{b}{(b^2 + a^2)^{1/2}} = \cos \phi \quad ,$$

and

$$\frac{a}{(b^2 + a^2)^{1/2}} = \sin \phi \quad ,$$

which at $\phi = 90^\circ$ are 0 and 1, respectively.

Therefore,

$$\frac{d\phi}{dT} = \frac{-\frac{db}{dT}}{(b^2 + a^2)^{1/2}} \quad \text{at } \phi = 90^\circ \quad . \tag{22}$$

But from eq. (21), $a = \omega_n^2$ and $b = Q(\omega_n^2 - \omega^2)$.

Therefore,

$$\frac{db}{dT} = \frac{dQ}{dT}(\omega_n^2 - \omega^2) + 2Q\omega_n \frac{d\omega_n}{dT} \quad ,$$

and

$$\frac{d\phi}{dT} = \frac{\frac{dQ}{dT}(\omega^2 - \omega_n^2) - 2Q\omega_n \frac{d\omega_n}{dT}}{\left[(\omega_n^2)^2 + Q^2(\omega_n^2 - \omega^2)^2\right]^{1/2}} \quad . \tag{23}$$

But operating around $\omega_n = \omega$, $\omega_n^2 - \omega^2 = 0$.

Therefore,

$$\frac{d\phi}{dT} = -\frac{2Q\frac{d\omega_n}{dT}}{\omega_n} \quad \text{at} \quad \phi = 90^\circ \quad . \tag{24}$$

The rate of change of the sensor natural frequency is 0.0015 Hz/C$^\circ$ as taken directly from the test data; therefore, with a Q of 295

$$\frac{d\phi}{dT} = -\frac{2(295)(0.0015)}{2.08} \text{ rad/C}^\circ \quad ,$$

or

$$\frac{d\phi}{dT} = -0.425 \text{ rad/C}^\circ = -24.4^\circ/\text{C}^\circ \quad . \tag{25}$$

This is the slope of the phase versus temperature curve at 90°. An actual temperature shift of 1°C causes $\approx 18^\circ$ phase shift on the signal.

- AMPLITUDE SHIFT

Since the slope of the amplitude versus frequency curve is zero at the resonant frequency, there is no amplitude shift due to $d\omega_n/dT$. There is, however, an amplitude shift due to dQ/dT.

Since the equivalent sensor output will vary with Q

$$\Gamma_{out} = \frac{\Gamma_{in} Q}{Q_o}$$

$$\frac{d(\Gamma_{out})}{dT} = \frac{\Gamma_{in}}{Q_o} \frac{dQ}{dT} = \Gamma_{in} \frac{-6.05}{295} = -0.0205\ \Gamma_{in} \tag{26}$$

$$= -2.05\%/^{\circ}C \text{ at } Q = 295$$

- VOLTAGE-TEMPERATURE SENSITIVITY

The change in voltage output is an additional amplitude shift with temperature. Expressed in percent, it is simply

$$\frac{\frac{dV}{dT}}{V_o} = \frac{0.0154}{1.33} = -1.16\%/^{\circ}C \quad . \tag{27}$$

- TUNED SENSOR VARIATION WITH TEMPERATURE

All the above calculations can be made with the tuned sensor parameters with the results being modified from the untuned sensor results by the difference in Q and Q slope; i.e.,

$$\frac{d\phi}{dT} = \frac{2Q \frac{d\omega_n}{dT}}{\omega_n} = \frac{-2(170)(0.0015)}{(2.08)} = 0.245 \text{ rad}/^{\circ}C = 14^{\circ}/^{\circ}C \tag{28}$$

and

$$\frac{\frac{dQ}{dT}}{Q_o} = \frac{2.8}{170} + 1.65\% \quad .$$

These drift rates are summarized in Table III.

TABLE III

AMPLITUDE AND PHASE ANGLE DRIFTS WITH TEMPERATURE

Sensor Condition	Phase Angle Drift, per °C	Amplitude Drift		
		Voltage, %/°C	Q, %/°C	Total, %/°C
Untuned	24.4°	-1.16	-2.05	-3.21
Tuned	14.0°	-1.16	+1.65	+0.49

2. Gravity Driven Noise and Drift Test

In order to demonstrate the stability of an actual output signal, the sensor was placed in its vacuum chamber and suspended inside a rotating proof mass system known as a "gravity generator." This test setup is shown in Fig. 19.

The gravitational signals are generated by two 15.5 kg masses on a rotating turntable. The masses rotate about the sensor and the gradients of their gravity field excite the sensor at twice the rotation speed. When the sensor is centered between the masses this provides an exact simulation of the gradiometer's gravitational detection method but the necessity of rotating the gradiometer is obviated, thus eliminating those sources of noise due to the sensor rotation.

The generator masses are separated by 18 in. center-to-center.

The dynamic driving gradient generated at the center of the sensor is therefore

M7642

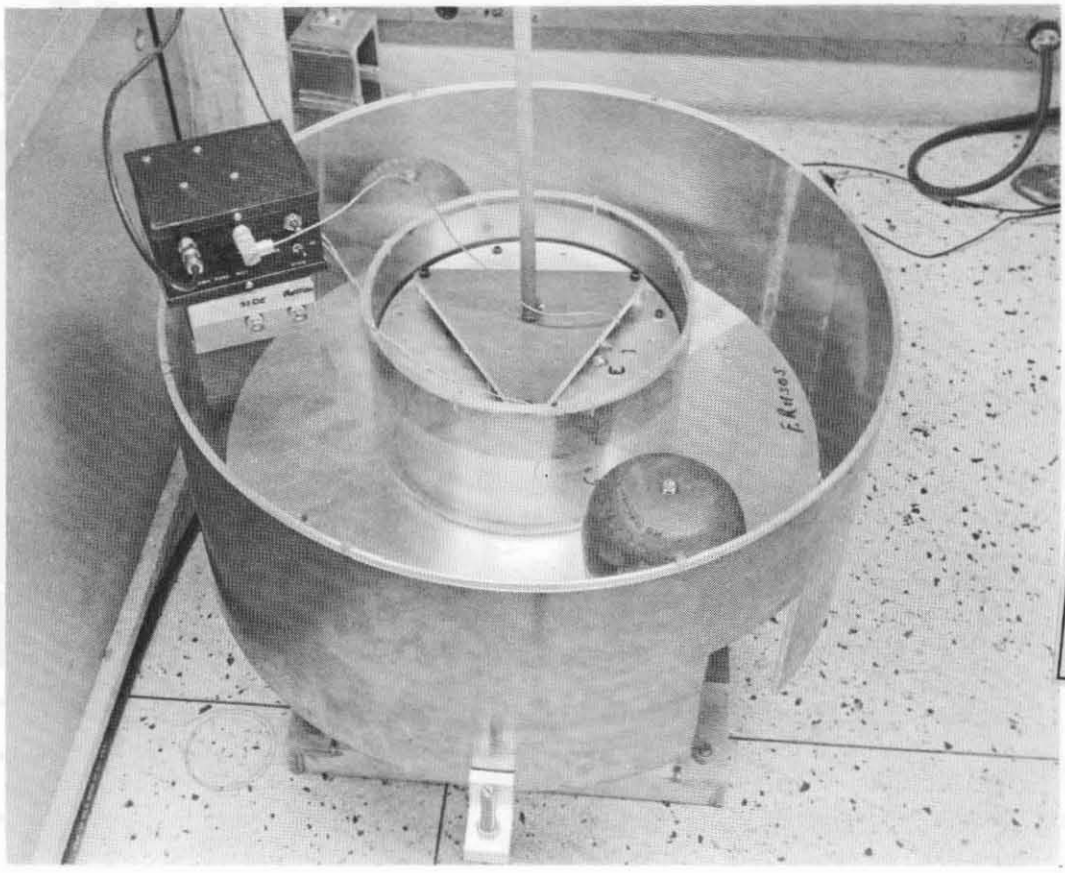

Fig. 19. Gravity Generator Test Setup.

$$\Gamma_{driving} = \frac{3GM}{R^3} = \frac{3(6.670) \times 10^{-8} \times (31,000)}{[(9)\ (2.54)]^3} = 523 \text{ E.U.} \qquad (29)$$

Prior to running the stability test, the masses were rotated through resonance and a sensor Q curve was obtained. This curve is shown in Fig. 20. The Q was determined to be 205, with no tuning circuit attached to the sensor.

The difference between the Q of this test and the Q as measured in the earlier temperature tests was not explained. It is possible that the aging of the epoxy used to bond the transducers to the flexure caused enough variation in the sensor damping to alter the Q. In any case, this Q test was repeated several times with the measured Q always falling near 200.

Inphase and quadrature sensitivity drift curves are shown in Figs. 21 and 22. These test curves were run for 44×10^3 sec. $\approx$ 12 hours during the evening, to minimize building and personnel noise. They were run on two different nights, but there was no change in the test setup between the two. Both curves have the same scale factor which can be evaluated by using the amplitude curve (inphase) where the 523 E.U. signal causes 7.2 cm deflection on the graph.

The scale factor is therefore:

72.6 E.U./cm or 7.26 E.U./mm,

or in terms of transducer output voltage since 1 cm = 1/50 mV on the transducer, the scale factor is 276 nV/E.U. The noise level of each curve can be evaluated using the area integration technique. The noise level is evaluated by noting that the area between a random noise curve and its mean equals $\sigma/\sqrt{2\pi}$ when the area is normalized to one-half. For a noise trace "a" centimeters long, the standard deviation on the noise is given by

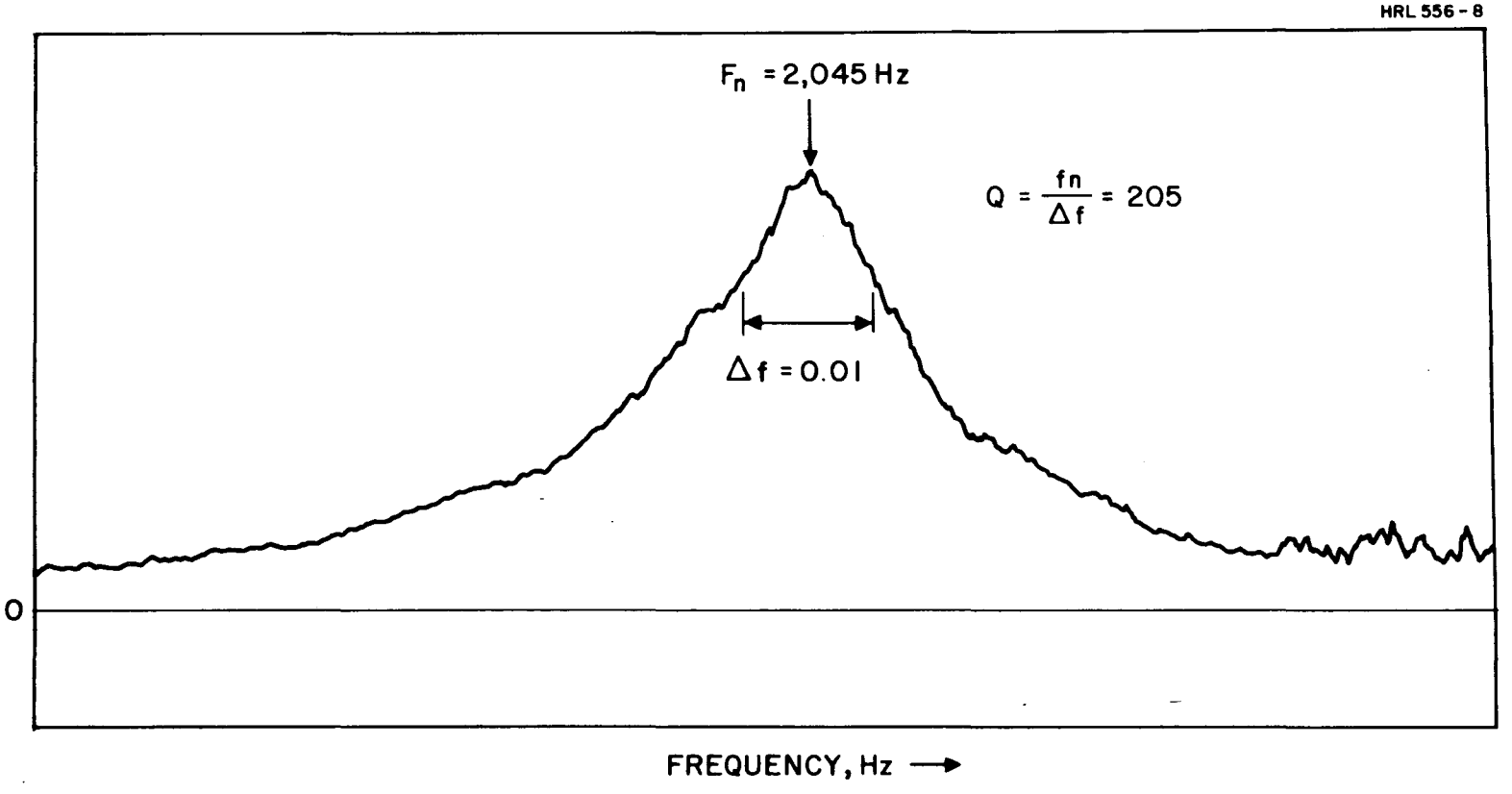

Fig. 20. 2 Hz Q Curve (no inductor).

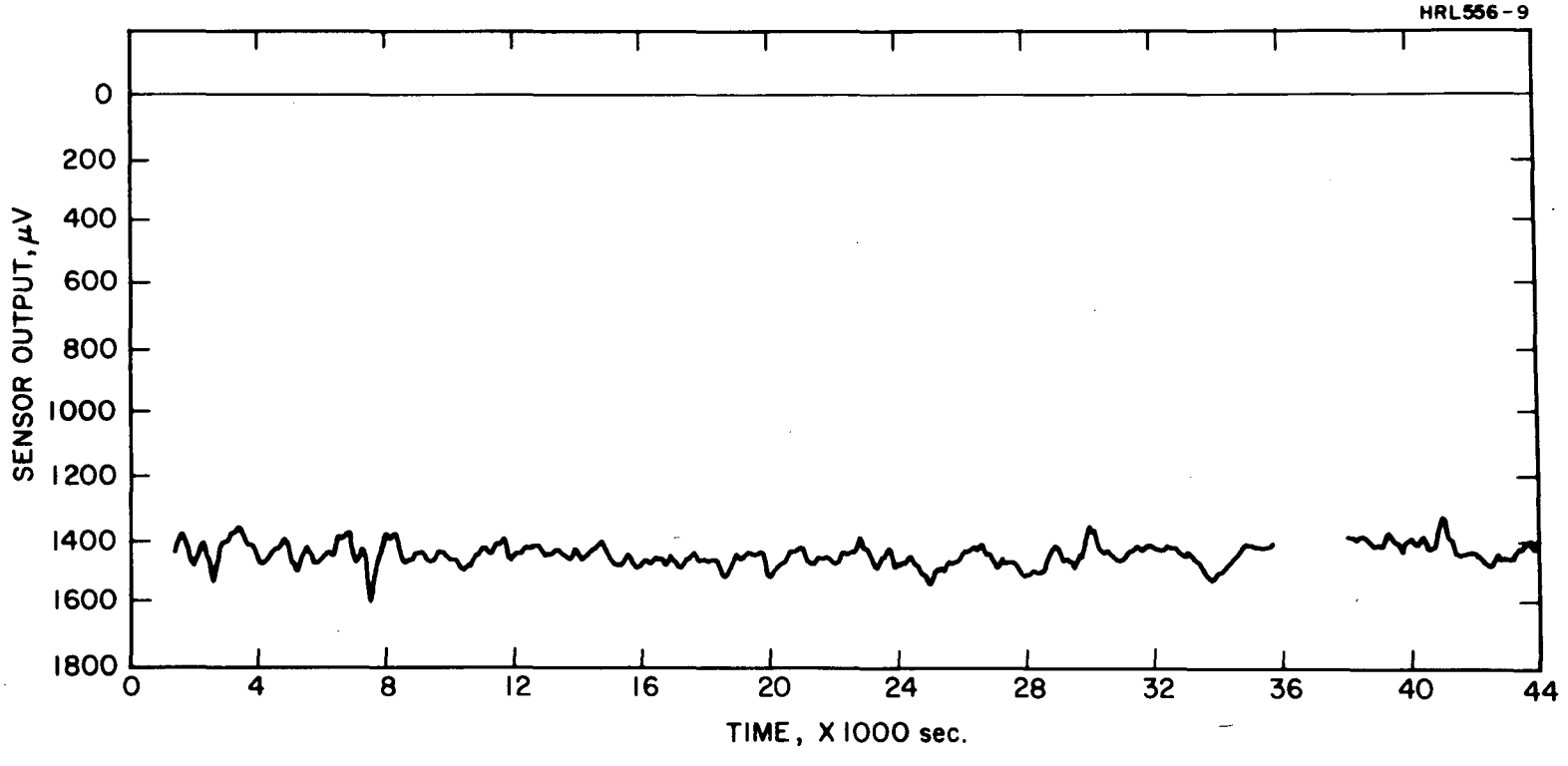

Fig. 21. Sensor Drift Test — Inphase.

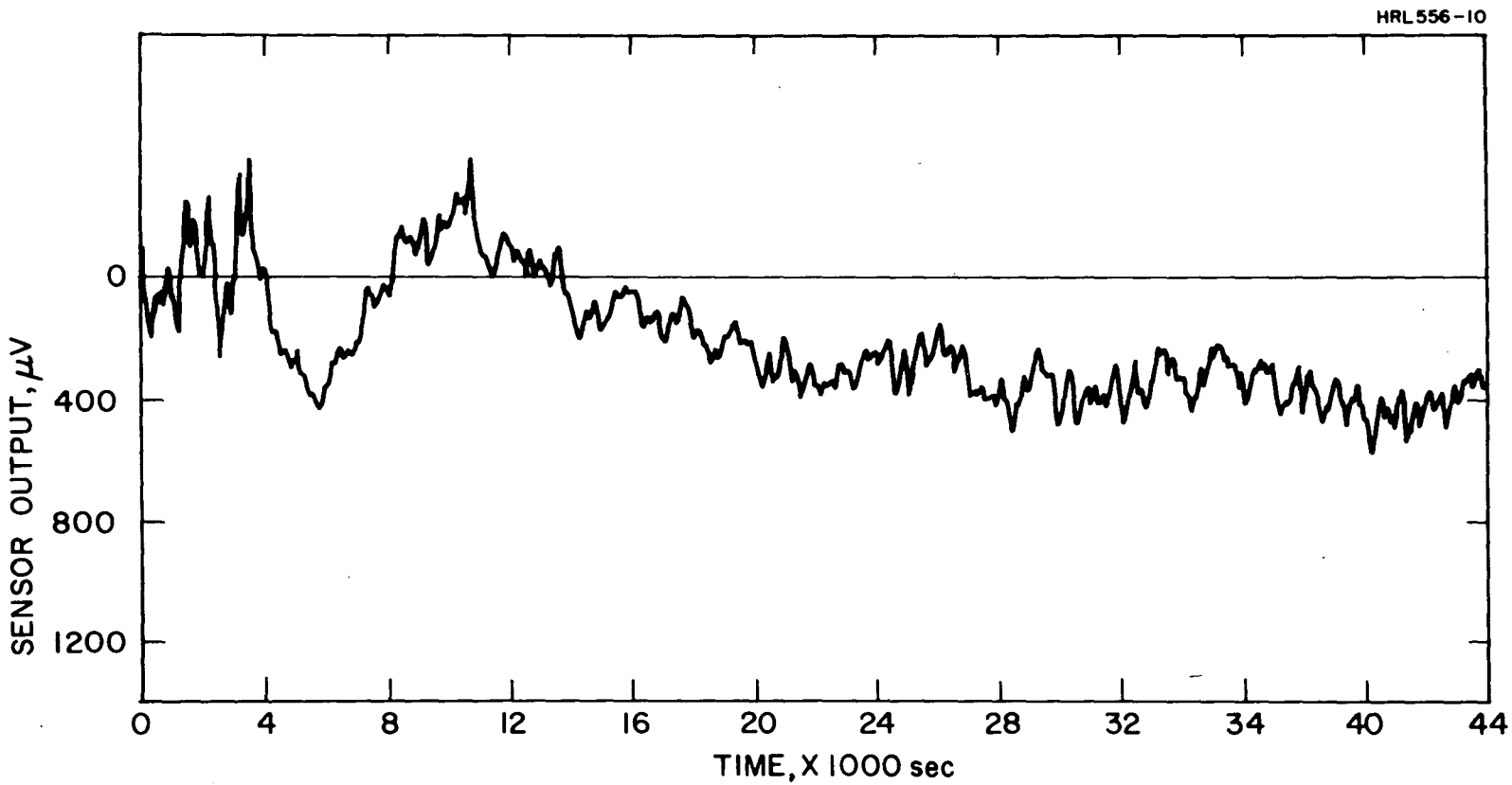

Fig. 22. Sensor Drift Test — Quadrature.

$$\sigma = \frac{\pi}{\sqrt{2}} \frac{A}{a} ,$$

where A is the area between the curve and its mean.

In this case a = 21 cm and

$$A_{inphase} = 0.66 \text{ cm}^2$$

$$A_{quadrature} = 1.145 \text{ cm}^2 .$$

Therefore,

$$\sigma_{inphase} = 0.03935 \text{ cm}$$

and

$$\sigma_{quad} = 0.0685 \text{ cm} ,$$

or multiplying by the scale factor of 72.6 E.U./cm

$$\sigma_{inphase} = 2.9 \text{ E.U.}$$

$$\sigma_{quadrature} = 5.0 \text{ E.U.} .$$

Linear drift on the inphase curve can also be evaluated as 5 mm/12 hours or

36.3 E.U.

5(7.26)/720 min = 0.0504 E.U./min.

These drift figures may now be reflected back with the aid of the temperature sensitivity data to determine the equivalent temperature drift which could have caused these errors.

• TEMPERATURE DRIFT

With 36 E.U. drift in 12 hours or $36/523 \cong 7\%$ of the signal, it would take a room temperature shift of just over $1.6^{\circ}C$ over the evening to cause such an output shift. This assumes a Q of 195 with the untuned Q drift versus temperature $6.05/^{\circ}C$ or $\frac{dQ}{dT}/Q_o = 3.1\%/^{\circ}C$; this added to the voltage shift of $-1.2\%/^{\circ}C$ = a total shift of $-4.3\%/^{\circ}C$. This appears to be a reasonable value for temperature change inside the building from 5:00 p.m. to 5:00 a.m.

The quadrature temperature drift is caused by signal phase angle shifting. About the sensor resonance (Q = 195), this equals $\approx$ 14 degrees/$^{\circ}C$. Referring to the Fig. 22 curve, the straight line drift for the 12 hour period was 2.2 cm = 160 E.U. This is equivalent to a phase shift of

$$\sin \theta = \frac{160}{523} = 0.306$$

$$\theta = 17.8^{\circ} \quad .$$

Although the phase shift curve is not linear, the linear approximation should be accurate enough for our purposes and the 12 hour temperature shift would equal

$$\Delta T = 1.3^{\circ}C \quad .$$

This is close to the estimated 1.6° temperature shift evaluated from the inphase data.

The initial dip and rise in the output curve can be explained by a drop in temperature of $1.2^{\circ}C$ followed by a rise of $0.7^{\circ}C$ and finally the slow drift down of $1.3^{\circ}C$ previously mentioned.

However, temperature effects alone do not explain the noise levels superimposed on the drift. Although the quadrature noise is higher than the inphase noise level, it is not high enough to account

for all the observable noise on the output signal. The difference in noise levels may be explained by temperature fluctuations, but the base noise level in the inphase channel must be largely due to noise from additional sources.

- ADDITIONAL NOISE SOURCES

The primary additional source of noise in the sensor test setup was noise induced in the sensor by lateral vibration. Because the sensor was not accurately balanced during assembly, it possessed some lateral acceleration sensitivity.

Isolation of 2 Hz acceleration inputs from the sensor proved to be a difficult task. Two basic methods of suspension were tried.

(1) The sensor was suspended from the ceiling I-beams by an eight foot long amber latex tube. Although the tube provided good high frequency isolation, it could not satisfactorily isolate out the low frequency excitation and the tube itself was subject to excitation at 2 Hz by air currents in the room. Various types of wind shields were used around the tube but the results were not satisfactory.

(2) The second method of suspension was to mount the sensor on a rod, which in turn was attached to a heavy stand made up of two columns and a cross beam. This method of suspension reduced the sensor noise level by a factor of four.

Some of the remaining noise was still attributable to input vibration.

Because of independent work completed recently at HRL, we now have a method of performing accurate arm balancing (both mass and inertia), thereby reducing acceleration sensitivity. Additional experimental work performed on this or similar sensors should be preceded by arm balancing.

3. Discussion of Results

Sensor drift levels are largely attributable to temperature shifts which affect the sensor output in both amplitude and phase.

Although the sensor signal phase is the most significantly affected by temperature, the effect of this drift on the data in a lunar mapping experiment will not be critical, as such an experiment was proposed to require only amplitude information from the sensor.

Phase angle accuracy as well as amplitude accuracy can be improved by decreasing the sensor Q and raising the sensor resonant frequency.

The noise levels below those produced by temperature drift are apparently caused by acceleration sensitivity due to arm unbalance and excited by low frequency motions of the sensor support system. We now have sensor arm balancing methods which will easily reduce this noise level by more than two orders of magnitude. In addition, raising the natural frequency to 6 Hz would increase noise attenuation another order of magnitude because of the low frequency supporting structure.

D. PERTINENT NONCONTRACTUAL TESTING

On May 25th and 26th 1971, additional noise tests were performed on the 2 Hz sensor. The goal of these tests was to eliminate the noise generated by air transmitted (acoustic) forces. This was accomplished by installing the sensor, mounted on a latex tube vibration isolation suspension, in a large vacuum tank and reducing the pressure in the tank down to 30 microns Hg.

Although the acoustic noise was eliminated, the data still showed noise generated by external room vibration, although attenuated considerably by the isolation suspension.

The resultant noise curve for this test is shown in Fig. 23. The rms noise level here is 5.2 E. U. (equivalent) which is a factor of 4 to 8 improvement over the data shown in Figs. 21 and 22 for an equivalent time constant.

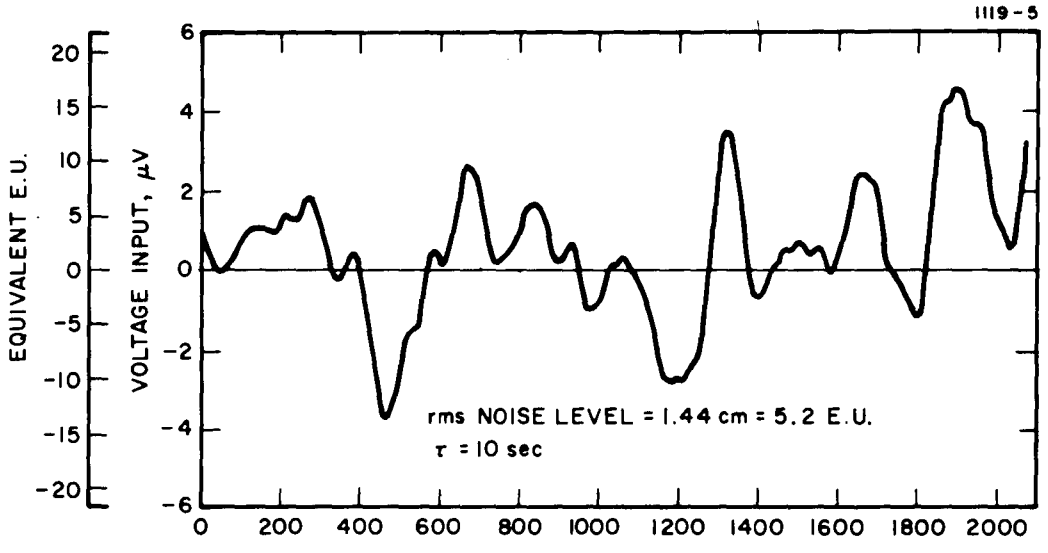

Fig. 23. Acoustically Isolated Sensor Noise Level.

SECTION IV

CONCLUSIONS AND RECOMMENDATIONS

A. CONCLUSIONS

The primary conclusions that can be drawn from the experiments are as follows.

1. Transducer Material

Of the three materials tested, there seems to be no difference in the change of output with temperature.

Bonding of the transducer to the supporting leaf appears to be critical to obtain repeatable results. However, this problem was not studied in depth.

2. Vertical Versus Horizontal Orientation

No difference was noted in temperature test results, when the sensor torsional axis was changed from vertical to horizontal.

3. Tuning Circuitry

Although the addition of the 37,000 H choke across the sensor output did not provide a significant improvement in signal-to-noise ratio we can extrapolate a factor of ten improvement if both strain transducers were operable. Drift in sensor Q as with temperature did seem to be minimized with the addition of the tuned circuit.

4. Noise

Sensor noise level was from 2 to 4 E. U. using a 100 sec integration time.

The 4 E. U. noise level of the quadrature channel is in part attributable to the temperature fluctuations of the sensor, while the fluctuations of the inphase channel are mainly assignable to the vibration noise coupled in through sensor arm unbalance.

Additional tests which eliminated acoustic vibration input reduced the sensor noise level to 5 E. U. at 10 sec integration time. This residual was assigned to mechanical vibration inputs which could be reduced by arm balancing.

B. RECOMMENDATIONS

Use of the tuned circuit combined with a flexure redesign which will provide more transducer area and a stiffer pivot should be sufficient to lower the sensor Q, when tuned, to below 60, reduce the slope of Q with temperature, and raise the natural frequency up to 6 Hz. These changes would ease the stringency of the preamplifier design, reduce the acceleration sensitivity under soft mounted conditions, and reduce the noise and drift due to temperature fluctuations.

The addition of temperature control on the sensor good to $\pm 0.1^{\circ}C$ would also aid in controlling noise and drift. We can estimate the expected error in signal amplitude, in a lunar application (input gradient 2700 E. U.) with the above parameters, for a $0.1^{\circ}C$ shift in temperature. For this estimate we will assume the same percentage shifts in Q and voltage as in the experimental data (total amplitude drift of $+0.49\% / ^{\circ}C$). This would imply a signal change of $0.0049 \times 2700 \times 0.1 = 1.35$ E. U. for a $0.1^{\circ}C$ temperature shift, or for random temperature fluctuation 0. 955 E. U. rms. Since $0.1^{\circ}C$ does not represent the best temperature control achievable, this noise level could be improved still further with tighter temperature control.

APPENDIX

SIMULATED TERRAIN MAPPING WITH THE ROTATING GRAVITY GRADIOMETER*

by

Curtis C. Bell
Robert L. Forward

Exploratory Studies Department
Hughes Research Laboratories
Malibu, California

and

Harvell P. Williams

National Aeronautics and Space Administration
Huntsville, Alabama

ABSTRACT

We present the results of an experimental simulation of the gravity gradient profile that we expect to obtain from a rotating gravity gradiometer passing over terrain with subsurface density fluctuations. The simulation was carried out by constructing a scaled down simplified model of the terrain with density variations similar to those expected in the real terrain. The model was moved past our laboratory version of the rotating gravity gradiometer and the output of the sensor was plotted as a function of the relative position of the sensor with respect to the simulated mass distribution. The resultant gravity gradient profile is compared with that predicted by our computer program for the same configuration. The situation simulated in the experiment was that of a lunar spacecraft at 30 km altitude orbiting over various mascon structures. Because of the $1/R^3$ characteristic of the gravity gradient, however, the simulation could apply equally to an aircraft at 3 km altitude flying over large geological structures many kilometers down, or an aircraft at 300 m altitude looking at small local structures near the surface.

INTRODUCTION

For the past several years we have been engaged in the development of a unique gravity gradiometer capable of measuring gravitational anomalies while remaining insensitive to accelerations.[1-6] Starting in a brand new field where the available technology was extremely limited, we have developed a laboratory model of our gradiometer capable of measuring gradients with accuracies in the 10^{-8} sec^{-2} to 10^{-9} sec^{-2} range (10 E.U. to 1 E.U.).[7] We have arrived at a stage of instrument development where further design modifications and improvements depend on the desired application of the sensor.[8-11]

One of the primary areas of application is that of determining the gravitational field of the moon.[11] Orbital analysis of satellites provides some information, but it cannot provide detailed data on localized anomalies. The rotating gradiometer is the first device which has demonstrated sufficient sensitivity to measure the extremely small forces involved in gravity gradiometry, and yet has a design which is sufficiently rugged for operation in either an orbital or an earthbound environment. This advantage in design enables the sensor to be demonstrated and calibrated in the laboratory prior to operation in an orbiting satellite.

This paper discusses the operating method of the gradiometer and the results of an experiment to demonstrate, on earth, the sensor's capabilities in lunar gravity measurement from orbit. In addition, a design for an orbiting selenodesy satellite is described.

THEORY OF SENSOR OPERATION

The instrumentation used in the experimental demonstration is the Hughes rotating gravitational gradient sensor. A laboratory model of this instrument is shown in Figure 1, and a schematic of the method of operation is shown in Figure 2.

*The work reported herein was partially supported under National Aeronautics and Space Administration Contract NAS 8-24788.

M 5704

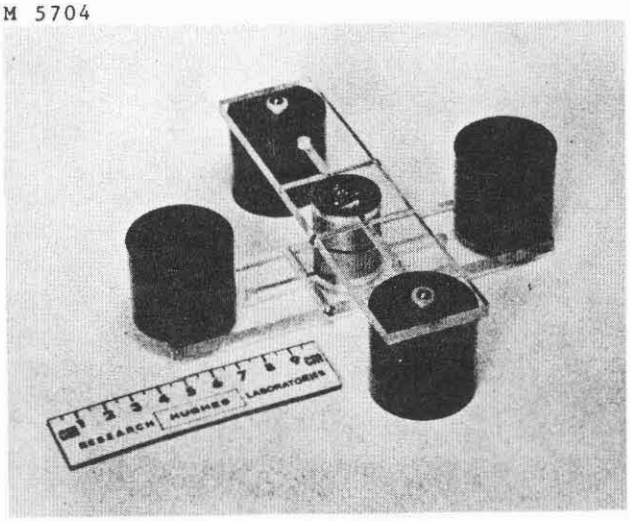

Fig. 1. Torsional gravity gradiometer.

D750-6R1

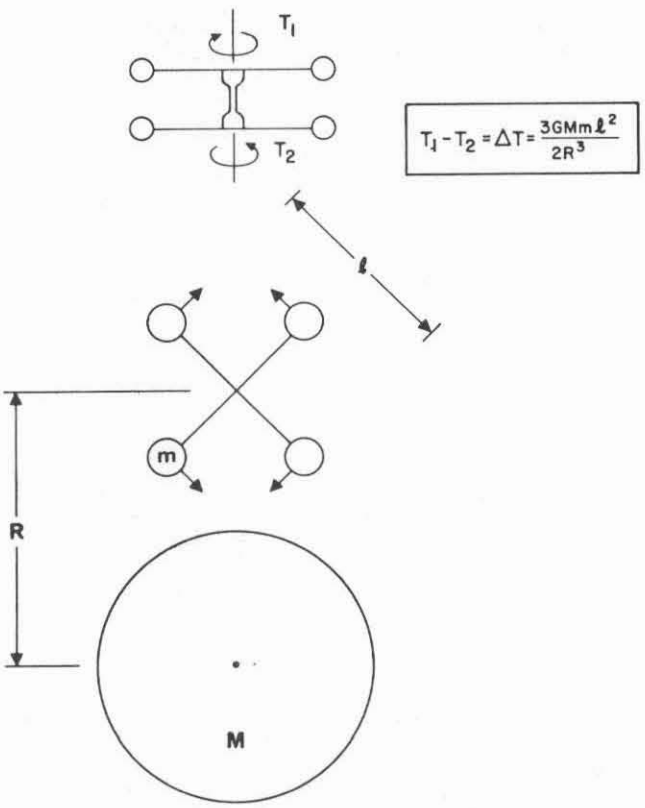

Fig. 2. Torsional gradiometer in free fall.

The basic concept of the rotating gravitational gradient sensor is as follows. If a system of proof masses is rotated in the static gravitational field of an object, the gravitational force gradient of this field will induce dynamic forces on the proof masses with a frequency which is twice the rotation frequency of the system, while inertial effects caused by accelerations of the proof mass mounting structure will induce forces with a frequency at the rotational frequency. The strength and direction of the gravitational force gradient can be determined independently of the inertial forces by measuring the amplitude and phase of the vibrations induced in these proof masses at the doubled frequency. Analysis shows that the sensing of the gravitational gradient will still occur if the proof mass system is in free fall.(3) More specifically, the proof mass system used is a system of masses coupled together with springs in a geometry which becomes a rotating differential angular accelerometer (see Figure 2).

In general, the gravitational field potential at a distance R from a mass point M is given by

$$\phi = -\frac{GM}{R} \qquad (1)$$

where the universal gravitation constant $G = 6.67 \times 10^{-11}\ m^3/kg\ sec^2$. The second order gradient of the gravitational potential is given by the symmetric tensor:

$$\Gamma = \nabla(\nabla\phi) = \begin{pmatrix} \frac{\partial^2\phi}{\partial x^2} & \frac{\partial^2\phi}{\partial y \partial x} & \frac{\partial^2\phi}{\partial z \partial x} \\ \frac{\partial^2\phi}{\partial x \partial y} & \frac{\partial^2\phi}{\partial y^2} & \frac{\partial^2\phi}{\partial z \partial y} \\ \frac{\partial^2\phi}{\partial x \partial z} & \frac{\partial^2\phi}{\partial y \partial z} & \frac{\partial^2\phi}{\partial z^2} \end{pmatrix} \qquad (2)$$

or, in Figure 2,

$$\Gamma = \begin{pmatrix} \Gamma_{xx} & \Gamma_{yx} & \Gamma_{zx} \\ \Gamma_{xy} & \Gamma_{yy} & \Gamma_{zy} \\ \Gamma_{xz} & \Gamma_{yz} & \Gamma_{zz} \end{pmatrix} = \frac{GM}{R^3} \begin{pmatrix} +2 & 0 & 0 \\ 0 & -1 & 0 \\ 0 & 0 & -1 \end{pmatrix} \qquad (3)$$

when the x axis is aligned along the radius R.

In operation, the sensor is rotated about its torsionally resonant axis at an angular rate ω which is exactly one-half the torsional resonant frequency. Only the differential torque ΔT between the sensor arms at the doubled frequency is coupled into the sensor output. This differential torque is given by[7]

$$\Delta T = \frac{m\ell^2}{2} \left[(\Gamma_{yy} - \Gamma_{xx}) \sin 2\omega t + 2\Gamma_{xy} \cos 2\omega t \right] \quad (4)$$

where ℓ is the characteristic length of the sensor, and m is the mass at the end of the sensor arms.

From (4) it can be seen that measurement of the in-phase and quadrature components of the sensor response with respect to some reference direction will provide a measure of certain components of the gravity gradient tensor. The particular components measured will depend upon the orientations of the sensor spin axis and the phase reference direction. An orthogonal triad of measurements at a point is sufficient to obtain all the components of the gravity gradient tensor. For the simple example shown in Figure 2, the differential torque induced by the mass M at the distance R is

$$\Delta T = \frac{3}{2} \frac{GM\, m\ell^2}{R^3} \sin 2\omega t \quad . \quad (5)$$

The angular resonant deflection between the two quadrupoles of the sensor rotating at one-half its torsional resonant frequency $\omega_n = 2\omega$ with an associated quality factor Q is therefore[7]

$$\delta = \frac{\Delta T Q}{I\, \omega_n^2} = \frac{3GMQ}{R^3\, \omega_n^2} \sin \omega_n t \quad (6)$$

where $I = m\ell^2/2$ is the quadrupole inertia.

The angle δ is extremely small. Surface gradients produced by the moon (1800 E.U.) will produce angular deflections of $\approx 1 \times 10^{-7}$ rad in typical orbital torsional sensor designs ($Q = 60$, $\omega = 6$ rad/sec), while useful threshold signals of 1 E.U. produce angular responses of $\approx 5 \times 10^{-11}$ rad.

It is now necessary to transduce this mechanical motion into an electrical signal for processing and transmission. This is accomplished by using a flexural pivot as the torsional spring and affixing a barium titanate strain transducer to one of the flexural spring leaves (see Figure 3). These transducers have been found to be more than adequate for sensing these small strains.

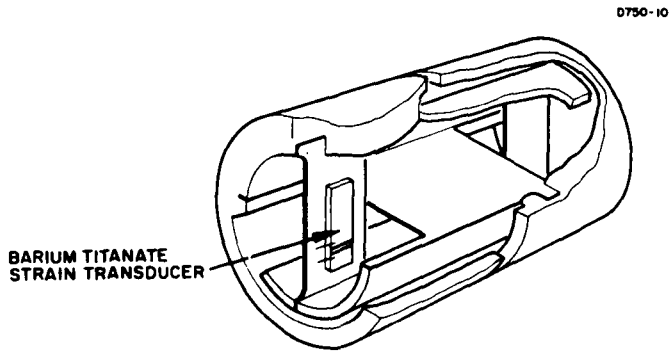

Fig. 3. Flexural pivot.

SELENODESY SATELLITE DESIGN[11]

In order to utilize this sensor for mapping the lunar gravity field from orbit, it is planned to use a spin-stabilized spacecraft whose spin speed is one-half that of the sensor resonance. The sensor is fixed to the spacecraft framework and the rotation required for the sensor operation is supplied by the spin of the spacecraft. This mode of operation has the advantage that the gravitational gradient field of the spacecraft is constant in the rotating reference frame of the sensor, and therefore does not contribute to the dynamic sensor response. Thus it is not necessary to calibrate the sensor to eliminate the background gradient bias signal of the spacecraft, as would be necessary for a static type of gradiometer.

The spacecraft design envisioned for the selenodesy satellite is a cylindrical structure 3.5 ft in diameter, 3 ft high, and with a total weight of 160 lb (see Figure 4). The satellite would have a nominal spin speed of 1 to 3 rps; the sensor would have a resonant frequency of twice the spin speed (2 to 6 Hz) and would be attached to the spacecraft at the center of mass with its torsional axis aligned along the spacecraft spin axis. The sensor package would be only slightly larger than the present designs, since the present designs have demonstrated adequate sensitivity for lunar mapping. The relatively large spacecraft size is dictated primarily by the size of the solar panel necessary to provide electrical power. For a fully redundant system, operating continuously and having a half-orbital time eclipse during which battery power must be used, the average power demand for the noneclipse part of flight is estimated at approximately 100 W; this requires 10 ft^2 of solar panel projected area.

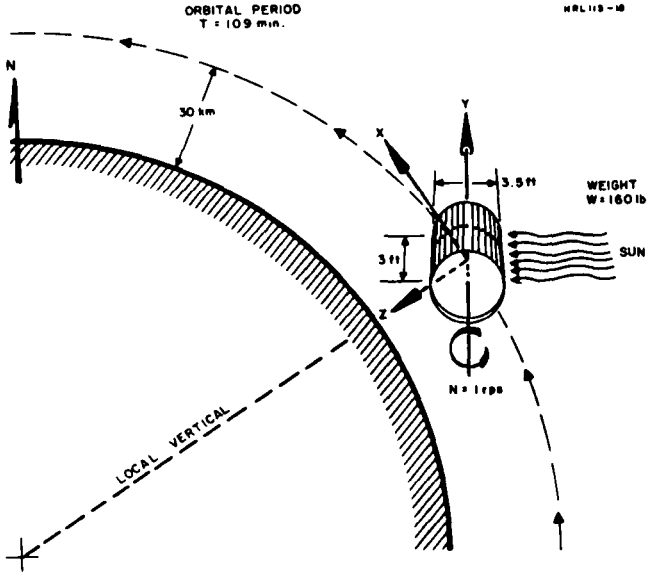

Fig. 4. Selenodesy satellite.

The most desirable orbital parameters for mapping the lunar surface would be to place the selenodesy satellite in a 30 km polar orbit with the orbital plane essentially parallel to the sun vector. The rotation of the moon under the satellite orbit causes the ground tracks of a 30 km polar orbit to be spaced 31 km apart at the lunar equator. Because the directional response of the sensor (or any gradiometer) is quite broad, the measurement at any time will be an average of the sensor response to those masses on the surface with a region whose diameter is approximately equal to the sensor altitude. Thus the ground track width of 30 km for a 30 km high orbit will give adequate coverage of the lunar surface near the equator and redundant coverage near the poles. (This can be used for periodic check of sensor calibration.) The mission duration would be one-half a lunar day, or 14 earth days. Lower orbits would greatly increase the resolution and sensitivity, but the measurements then would have to be taken over many lunar rotations in order to cover completely the surface area near the equator.

The desirable instrument integration time is also determined by the orbital parameters and the broad sensor response characteristic. Because the orbital speed $v = 1.62$ km/sec and the sensor resolution element is roughly equal to its altitude ($d = h = 30$ km), the time required for the sensor to pass through one resolution element is

$$t = d/v = 18 \text{ sec} \quad . \qquad (7)$$

This is the maximum usable integration time for good data at 30 km altitude. Shorter integration times (3 to 10 sec) would probably be used, but times much shorter than 3 sec would increase the data storage and transmission problem without appreciably improving the final resolution.

The planned selenodesy satellite system is based on the assumption that the satellite will be delivered and placed in the proper orbit by an Apollo spacecraft as part of its mission. Once the selenodesy satellite is spun up and placed in orbit, the Apollo spacecraft can continue with the remainder of its mission and the autonomous satellite will continue its operations with no further support from the Apollo spacecraft. The satellite design (see Figure 5) has its own electrical power system, an active attitude control system, a semiactive thermal control system, and a two-way communication system. The last utilizes a direct down-link to earth-based STADAN or DSIF stations for telemetry data transmission, plus an uplink for receiving ground commands, if desired.

The baseline system includes an electrical power subsystem capable of supporting both daylight and eclipse time operation. The solar panel is sized to provide adequate power for charging the batteries. Both charging and discharging are automatically controlled. Regulation is reduced to minimal, and electronic subsystems will be

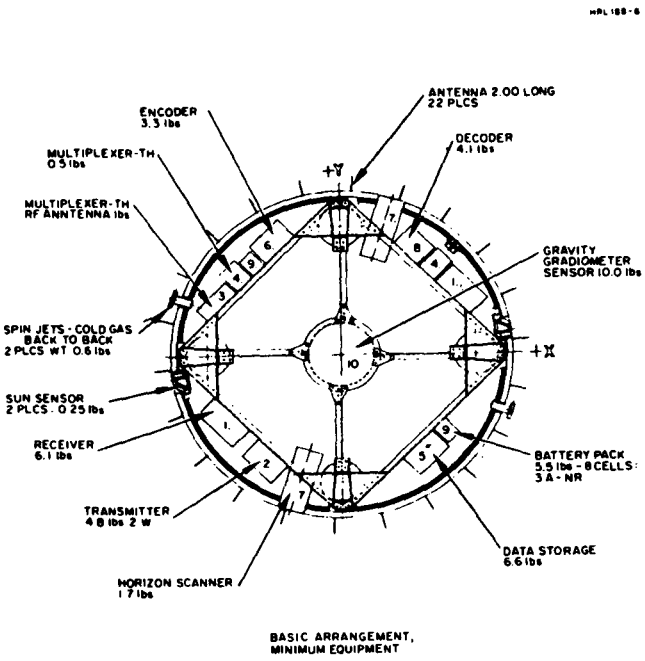

Fig. 5. Lunar selenodesy satellite.

supplied with 28 V dc ± 5%. Those components which may require better regulation are equipped with necessary provisions.

Attitude information will be derived from measurements of sun sensors and moon horizon crossing sensors mounted on the spacecraft. These data, acquired periodically, will be telemetered to the ground stations. Additional information, such as satellite orbital position and velocity, will be derived from ground tracking data and used in the attitude determination process.

The attitude control and spin-speed control are both effected with a cold gas reaction jet system. Because the baseline system does not include an on-board computer, all computations pertaining to attitude determination are expected to be performed on the ground. Any necessary corrections will be commanded by ground control centers. Very little disturbance of spacecraft nominal orientation is expected. The major source of disturbance torque will be solar pressure during the noneclipse part of flight. Ten square feet of projected area, assuming a pessimistic 0.1 ft CG-CP misalignment, will produce a torque of 10^{-7} ft-lb on the spacecraft. At that magnitude, considering a 40 ft-lb-sec spin axis angular momentum to resist disturbance, the 0.1° would have to be corrected once every 8 earthdays.

Separate thermal controls are provided, one for the gradiometer sensor capsule, and one for spacecraft internal space. Sensor environment will be maintained at 30 ± 1°C while spacecraft is controlled to nominal 20 ± 10°C. Electric heaters are employed to raise the temperature during eclipse flight. An adequate size thermal window at one end of the cylindrical structure is equipped with an aluminum radiator facing dark-space.

The telemetry and command system is designed for direct communication with ground stations. Electronic equipment is completely redundant. An all-solid-state transmitter operates at two power levels: high, approximately 1 W radiated power during telemetry data transmission; and low, less than 0.5 W when only a beacon signal is generated for tracking purpose. The communication link is designed for operation with an 85-ft ground antenna of STADAN or DSIF stations. All systems are S-band, sized for nominal 2 GHz. The spacecraft is equipped with quarter wave, whip-type antennas, the radially oriented whips being spaced half-wave around the equator portion of the vehicle, and axially oriented whips at periphery of one end.

The sequence of events for the gradiometer satellite is envisioned to begin with deployment from the spacecraft carrier. It is expected that a spacecraft carrier will place the experiment vehicle in proper orbit, with proper attitude and spinning at the required speed. System operational checkout should be performed prior to physical separation from the carrier vehicle.

From the time of release all the subsystems are expected to operate continuously. Gradiometer sensor data will be taken continuously and stored in digital form in onboard memory. Attitude sensor outputs and various engineering data will be sampled automatically at predetermined time intervals controlled by an onboard time clock. These data will be encoded and stored in core memory onboard the spacecraft, unless real-time transmission is commanded by ground control station.

Accumulated data will be transmitted to earth on command from designated ground stations. A limited number of command channels are provided to allow spacecraft attitude correction, additional sampling of attitude sensor outputs and other engineering data, switching of basic redundant components such as transmitter, receiver, batteries, etc. Most of this data taking is designed to provide information on sensor operational conditions and for trouble diagnostics. Except for attitude control through the reaction jet system, no active ground control of the experimental mission is contemplated.

THE LUNAR SIMULATION MODEL

One facet of the problem of demonstrating the feasibility of using the rotating gravity gradiometer for lunar orbiting selenodesy is to demonstrate as conclusively as possible, either by analytical models or by an experimental simulation, that the data produced by such a sensor will be valuable in determining the lunar gravitational field anomalies.

The most straightforward method for investigating the feasibility of the sensor would be to develop a complete analytical model for the sensor system and then run computer simulations against various analytical models of the lunar subsurface structure. To be complete, the analytical model should include not only the sensor parameters, but also possible sources of noise and error, such as thermal noise, gain drift, phase drift, nutational noise, amplifier noise, etc. This approach has the advantage of simplicity; however, because the model assumed can include only those sources of error that are known, and because real sensors may have other noise and error sources which are not discovered prior to actual operation, an analytical proof of feasibility is not as conclusive or convincing as an experimental simulation.

Fortunately, since a gravity gradiometer measures the gradient of the gravitational force field, which falls off as $1/R^3$, it is found that large-sized geophysical masses can be simulated by direct scaling of the test mass parameters (with the sensor size and mass held constant). For example, the gravity gradient of a 4 km high mountain measured by a sensor at an altitude of 20 km is the same as the gravity gradient of a 4 cm radius rock measured by the same sensor at a distance of 20 cm.

The direct simulation technique is equally applicable to any sensor and can be used to test any type of gradiometer capable of operating on earth under controlled laboratory conditions. The gradient simulation technique can be used to compare the relative performance of various sensors; check the predictions of the analytical models of the sensors against their actual performance; aid geophysicists in developing methods of handling, presenting, and processing the gradient data to produce the best estimate regarding the geological formations which caused the gradients; and measure the gradient fields of the more complex mass distributions which would take longer to calculate (because of their complex shapes) than to simulate experimentally.

The configuration of the flyby simulation experimental equipment used in our test is shown in Figures 6 and 7. The mechanical portion consists of a sensor and its isolation and drive mechanisms contained in a vacuum system, and a flyby track with drive motor, drive chain, mass carriages, and test masses. For convenience we used lead mass spheres rather than rock. The density fluctuations in real mascons or in geophysical formations are much smaller than those of lead, but the large densi difference implies a radius difference o only a factor of two between a lead and a rock sphere.

M 6840

Fig. 6. Mass flyby test setup.

The flyby track was placed 18.5 in. from the center of the sensor. The actual velocity of the masses on the flyby track was measured at just under 1 in./sec. The simulated velocity for a 30 km altitude therefore would be 1.6 km/sec (6000 km/hour) which is the orbital velocity of a 30 km lunar orbit. Although the simulation experiments were designed to demonstrate the feasibility of utilizing the sensor for orbital selenodesy, the simulation parameters are also relevant for the problem of airborne geodesy. The same laboratory parameters also simulate an aircraft flying at 600 km/hour at 3 km altitude. (Rather fast for airborne geophysical prospecting, but within the right range.)

M 6839

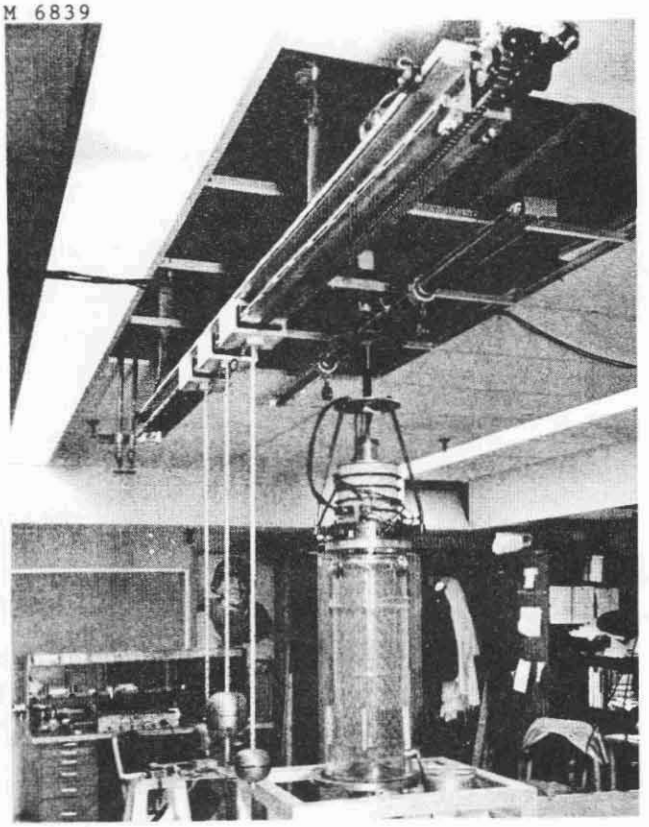

Fig. 7. Mass flyby drive and track.

In the laboratory tests the sensor was suspended by an elastic suspension from an iron rotor, which in turn was levitated by a servocontrolled magnetic bearing. Beneath, and coaxial with, the magnetic bearing solenoid is a pancake motor stator which applies the rotation torque to the rotor. The sensor is rotated at exactly one-half its resonant frequency by means of a servocontrolled asynchronous drive system using the stable reference frequency which is also used by the signal processing electronics. The sensor drive and data retrieval electronics are shown in block diagram form in Figure 8.

Signals from the barium titanate strain transducer are amplified and transmitted from the sensor to the receiving equipment outside the rotating system by means of an intermediate FM telemetry system. The received signal is demodulated and fed into a nulling circuit where that portion of the phase coherent signal due to the constant mass distribution of the laboratory, magnetic effects, and light pressure effects is biased out with a phase and amplitude adjusted portion of the reference signal.

This nulled signal is then fed into a two phase Princeton Applied Research lock-in amplifier (Model JB-6), which reads the coherent portion of the signal at twice the sensor rotation speed. The JB-6 can read the amplitude of this signal at any chosen phase angle with respect to the reference. A quadrature meter also reads the signal at 90° to this amplitude. The signals at 0° and 90° were added vectorially by the Cartesian to polar translator to determine the amplitude and phase of the sensor signal generated by the test masses. During the tests, three data outputs — amplitude, in-phase, and quadrature — were recorded on graph paper by three x-y plotters. These plots constitute the basic experimental data.

The frequency of the sensor used for the simulation was 32 Hz (rotation speed of 16 rps = 960 rpm). The Q was 400, which gave a sensor time constant of approximately 4 sec. The output of the sensor was passed through a two-stage 3 sec RC filter which increased the effective integration time to approximately 6 sec. The sensor for the selenodesy satellite would have a lower frequency and lower Q, but approximately the same integration time. Thus, these experimental simulations were run with signal processing parameters that were quite realistic, as there were definite effects on the data due to the finite delay and integration time of the sensor and its electronics, and the computer program had to take these time constants into account to fit the experimental data.

NOISE AND DRIFT TEST[11]

One of the tests run on the sensor was to simply measure the sensor output for approximately 1000 sec. Care was exercised to prevent any variations in the gravity field of the room (a person passing 3 ft away would add significantly to the sensor output). The amplitude data taken during this test are shown in Figure 9. The average slope of the curve is 1.4 E.U./min, which represents the general drift rate of the system. The drift is known to be caused by temperature variations in the magnetic levitation system, which cause the sensor to be raised or lowered slightly in the background gradient field of the room.

The standard deviation of the random noise superimposed on the linear drift was measured as

$$\sigma = 4 \text{ E.U. for } \tau = 3 \text{ sec} \qquad (8)$$

or

$$\sigma = 1.2 \text{ E.U. for } \tau = 10 \text{ sec.} \qquad (9)$$

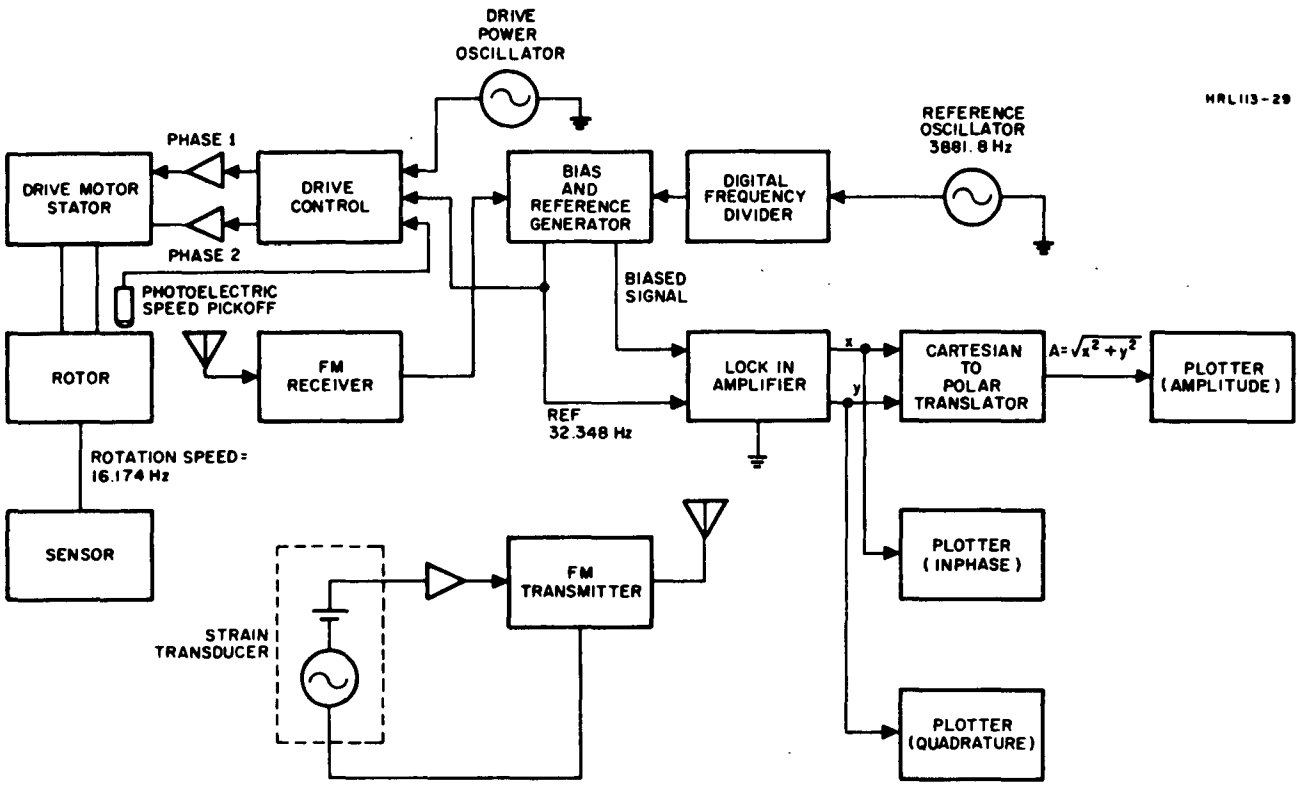

Fig. 8. System block diagram.

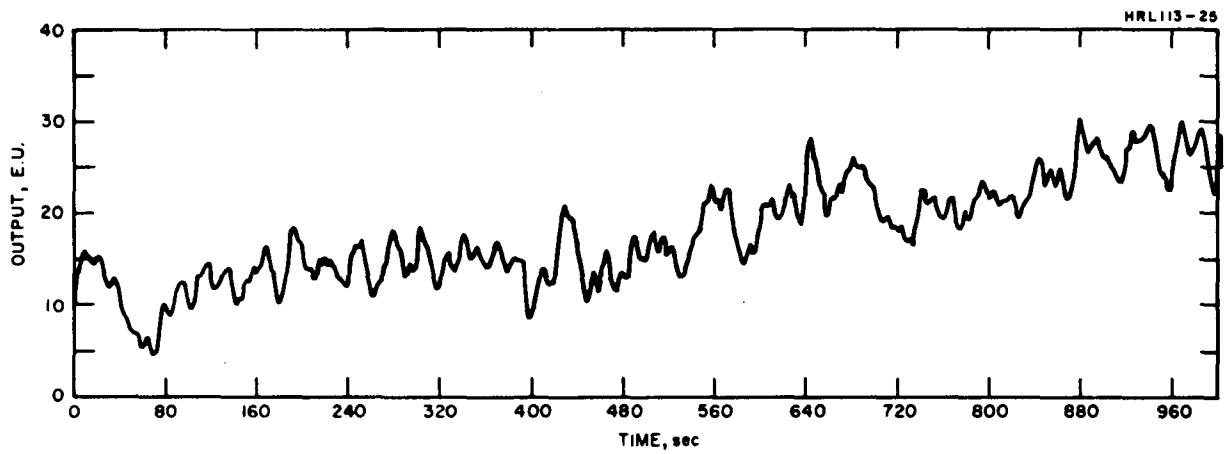

Fig. 9. Amplitude data.

FLYBY SIMULATION TESTS

Most of our tests on this program[11] were simulation tests of the sensor orbiting over various mass distributions at various distances. For each test the mass carrier was stopped at one end of its track and the mass spacing and position were adjusted to the desired configuration. The sensor bias then was adjusted to give a minimum response. Four runs, each about 85 sec long, were made, two in each direction, with no adjustment to the bias until the beginning of the next set of runs. The variations in the bias during the set of four runs usually were quite small, but even a few E.U. change could be identified easily when the experimental plots were compared with those predicted by the computer program.

In all of the following curves, the solid line is a trace of the recorder plots showing the output of the sensor as a function of time. The first curve is the amplitude of the sensor response, the second is the sine or in-phase response, and the third is the cosine or quadrature response. The dotted lines are a plot of the theoretical prediction of the sensor output with time. The computer program used to obtain the theoretical curves was developed in 1967 by D. Berman,[12] modified to include the effects of a finite sensor time constant and to provide a direct plot of the computer output. The bias levels used in the computer program to obtain the best fit to the experimental curves for the in-phase and quadrature channels are printed at the top of the plots. A difference of 1 E.U. usually gave a significant difference in fit to the experimental curve.

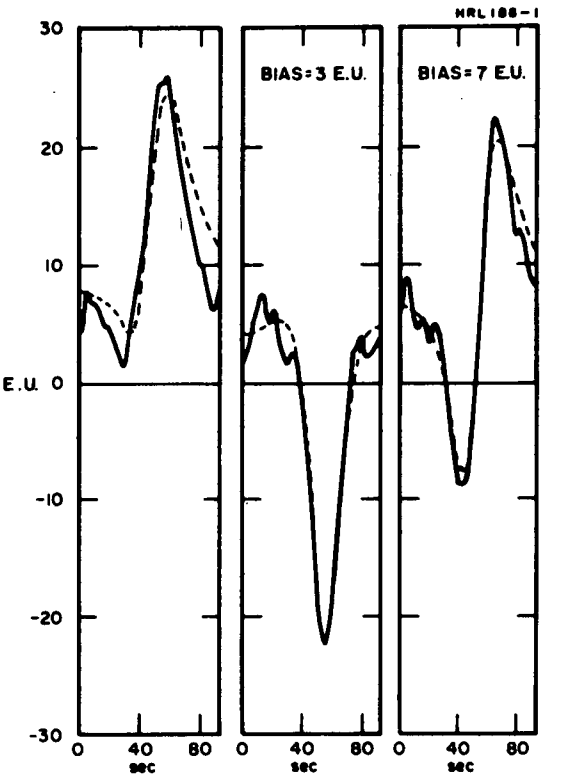

Fig. 10. Single mass flyby test.

Single Mass Flyby Test

A single mass (15.493 kg) was mounted on the center post of the mass carrier in the approximate rotation plane of the sensor and "flown by" the sensor. The test was repeated at 2 in. height increments above the sensor rotation plane to a final height of 18 in. The purpose of this test was to verify experimentally the $\cos^2\theta$ sensor response function for masses to one or the other side of the orbital track. The response to a single mass right on the orbital track is shown in Figure 10.

During these first tests the sensor support mechanism had not completed its warm-up, and there was considerable sensor bias in each channel. The computer response gave the best fit when the bias was assumed to be 3 E.U. in the in-phase channel and 7 E.U. in the quadrature channel. This relatively high residual bias level is the cause of the unusual shape of the amplitude curve, which without bias would be a simple single peaked curve, slightly skewed by the system time delay.

Two Mass Flyby (Horizontal Separation)

A second set of curves was taken with two approximately equal masses (14.386 and 15.493 kg) that were flown by in the plane of the sensor with horizontal separation distances x of from 18 to 24.5 in. (see Figure 11). As expected, it was easy to identify the separate peaks when the two masses were separated by more than the sensor distance (18.5 in.). The curve in Figure 12 shows the response for 24.5 in. separation. The response is not only double lobed, indicating that there are two masses, but the first lobe is a few E.U. lower, indicating that the first mass that passed was less massive than the second. When the separation was decreased to 18 in. (see Figure 13), however, it became difficult to determine from the sensor response whether there were two distinct masses. Theoretically, if there were a great deal of a priori information about the structure being observed, the response could be unfolded using the sensor response characteristics; practically, however, these experimental results demonstrate that the directional resolution of a gravity gradiometer is no better than that of a gravity meter, and that at 30 km from a mass distribution the resolution will be approximately 30 km.

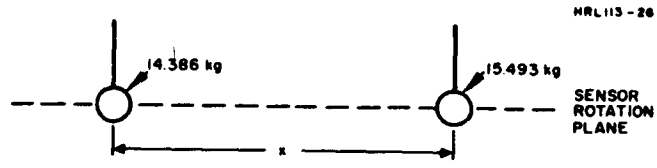

Fig. 11. Two mass flyby (horizontal separation.

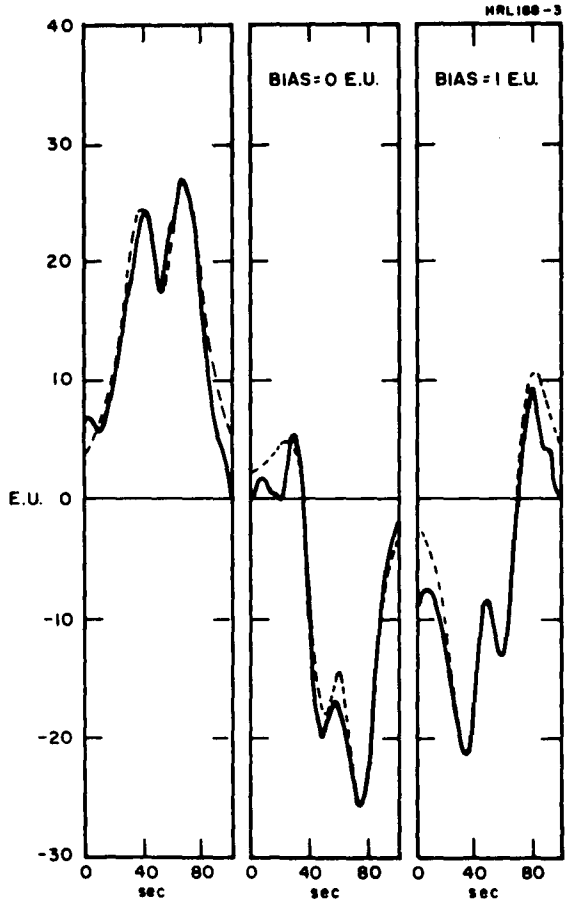

Fig. 12. Two mass horizontal separation flyby test (24.5 in. separation distance).

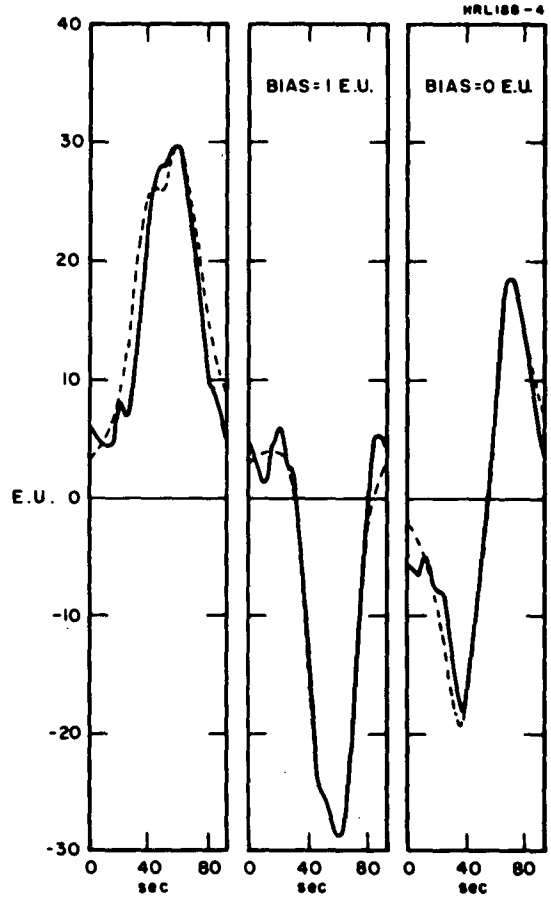

Fig. 13. Two mass horizontal separation flyby test (18 in. separation distance.

Three Mass Flyby

A system of three masses in a triangular array, simulating a more complex mass distribution (see Figure 14) was flown by the sensor at heights ranging from 0 to 18 in. at 2 in. intervals. The plane of the three masses was maintained at the fly-by distance of 18.5 in. from the sensor.

The data taken at h = 0, where the sensor passes first over the 5.66 kg mass and then over the 14.4 kg mass, are shown in Figure 15. The smaller mass shows up as a definite bump on the side of the response from the larger mass.

The plot for a sensor passing at 10 in. below the 5.66 and 14.4 kg masses (and 4 in. above the 15.5 kg mass) is shown in Figure 16. The response is similar to that from a single 15 kg mass, but detailed comparison with the single mass flyby curve (Figure 10) shows that it is broader, indicating a more complex mass distribution.

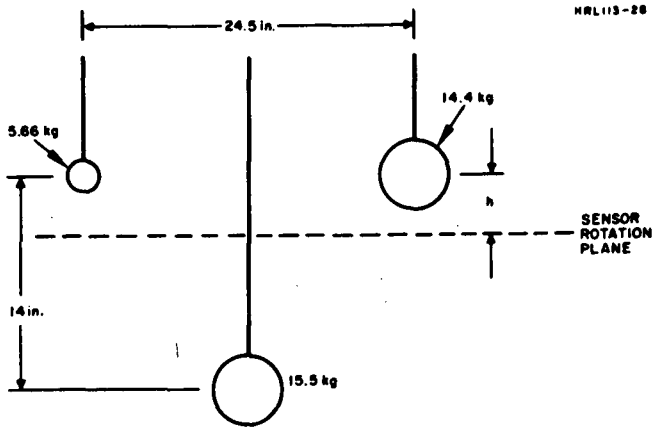

Fig. 14. Three mass flyby.

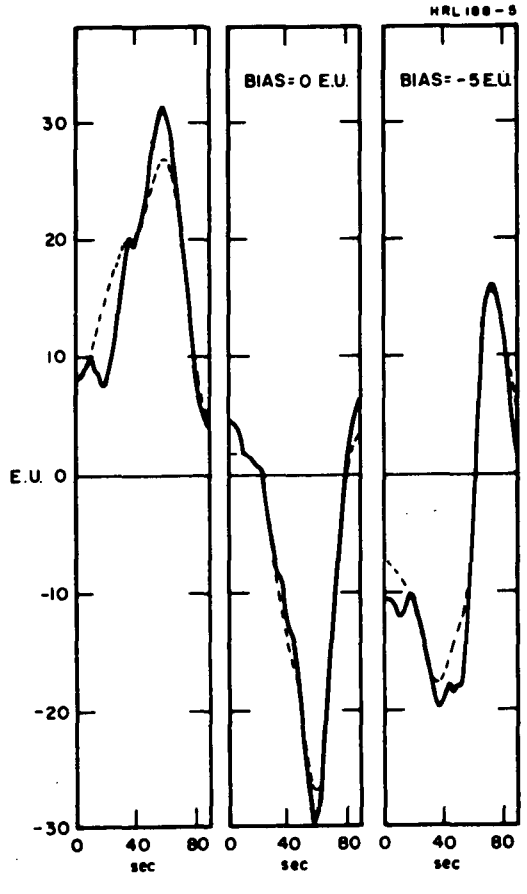

Fig. 15. Three mass flyby test (h = 0 in.).

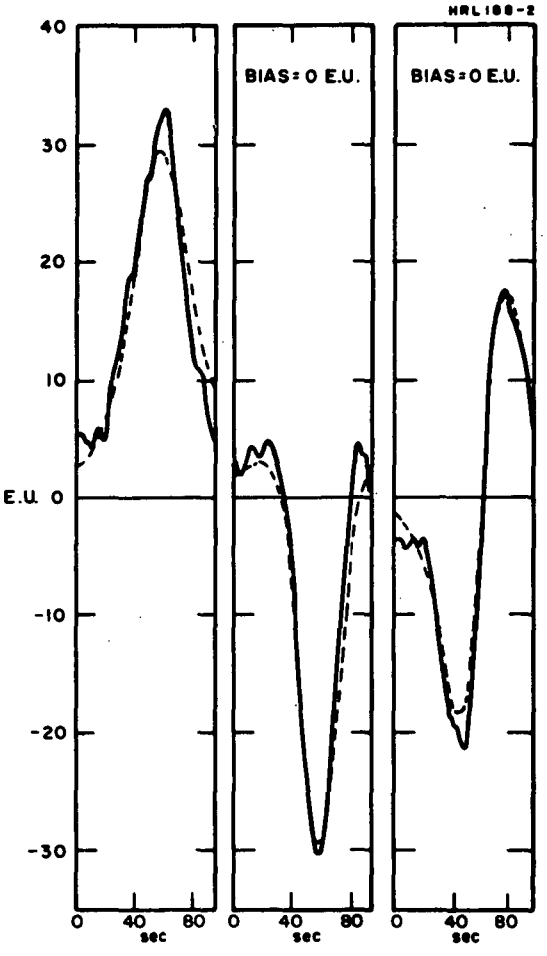

Fig. 16. Three mass flyby test (h = 10 in.).

CONCLUSIONS

The results of the noise and drift test, and the comparison of the experimental simulation tests with the theoretical predictions, confirm that the rotating gravity gradiometer is capable of extracting information about mascon distributions from lunar orbit, and that the present sensitivity of the sensor is adequate for lunar orbital selenodesy. The experimental work also verified our analytical and computer models(10-12) for the directional and time response of the sensor. These analytical models can be used to calculate the response of the sensor to various mass distributions and to determine the extent of the information obtainable concerning the mass distribution from measurements of the external gravitational gradient field. One recent example(10) was the verification for the Arms Control and Disarmament Agency that gravity gradiometer measurements around the warhead of a silo emplaced missile can determine the presence of multiple re-entry vehicles within the warhead shroud.

ACKNOWLEDGMENTS

The authors would like to thank Robert E. Steuri, Dale M. Sipma, Glenn F. Kloiber, Kenneth B. Craig, Ismael Charnabroda and Donald D. Boswell for carrying out the long and tedious 24 hour runs in the laboratory and on the computer to obtain the data required for this program, only a small fraction of which is shown in this paper.

REFERENCES

(1) Forward, R.L., "Mass Detector," Hughes Research Laboratories Internal Report RL-59, 19 March 1962.

(2) Forward, R.L. "Gravitational Mass Sensor," Proc. 1963 Symposium on Unconventional Inertial Sensors, Farmingdale, L.I., N.Y., 18-19 November 1963.

(3) Forward, R.L., "Rotating Gravitational and Inertial Sensors," Proc. AIAA Unmanned Spacecraft Meeting, Los Angeles, California, 1-4 March 1965, pp. 346-351.

(4) Bell, C.C., Forward, R.L., and Morris, J.R., "Mass Detection by Means of Measuring Gravity Gradients," AIAA 2nd Annual Meeting, San Francisco, California, 26-29 July 1965.

(5) Forward, R.L., Bell, C.C., Morris, J.R., Richardson, J.M., Miller, L.R., and Berman, D., "Research on Gravitational Mass Sensors," Final Report, NASW-1035, Hughes Research Laboratories, Malibu, California, 15 August 1966.

(6) Forward, R.L., "Measurement of Static Force Field Gradients," U.S. Patent 3,273,397, Filed 5 June 1964, Issued 20 Sept. 1966.

(7) Forward, R.L., Bell, C.C., Berman, D., Beard, T.D., and Miller, L.R., "Detection of Static Gravitational Force Gradient Fields with a Rotating Mass Sensor," Bull. Am. Phys. Soc., Vol. 12, p. 1127, 1967; Proc. Fifth Symposium on Unconventional Inertial Sensors, 28-30 Jan 1969, Brooklyn, N.Y.

(8) Forward, R.L., Pilcher, L.S., and Norwood, V.T., "Asteroid Belt Investigation Using Small, Spin-Stabilized Fly-By Probes," Proc. AAS Symp. on Planetary Geology and Geophysics, Boston, Mass., 25-27 May 1967.

(9) Forward, R.L., Bell, C.C., Berman, D., Miller, L.R., Harrison, J.C., Parker, H.M., and Hose, E., "Research Toward Feasibility of an Instrument for Measuring Vertical Gradients of Gravity," Final Report AF 19(628)-6134, Hughes Research Laboratories, Malibu, Calif., October 1967.

(10) "A Feasibility Study of MIRV Simulated Inspection by Gravity Gradiometry" Final Report ACDA/ST-171, Hughes Research Laboratories, Malibu, Calif., November 1969.

(11) Bell, C.C., "Lunar Orbiter Selenodesy Feasibility Demonstration," Final Report, NAS 8-24788, Hughes Research Laboratories, Malibu, Calif., January 1970.

(12) Berman, D., "Gravity Gradiometer Computer Model for Simulated Gradient Contour Mapping," REV. SCI. INSTR., Vol. 38, pp. 1433-1441, 1967.